A New Narrative for CO$_2$ Corrosion of Mild Steel

Aria Kahyarian [ORCID]*,z **and Srdjan Nesic**

Institute for Corrosion and Multi-phase Flow Technology, Ohio University, Athens, Ohio, USA

The conventionally accepted mechanism of CO$_2$ corrosion considers the direct reduction of carbonic acid as the main process that results in the higher corrosion rates as compared to that observed in strong acid solutions with the same pH. The present study is an attempt to further elucidate the underlying electrochemical mechanisms of CO$_2$ corrosion. In this regard, the mechanism of CO$_2$ corrosion was investigated based on the cathodic and anodic polarization behavior of mild steel in CO$_2$-saturated solutions at elevated pressures. The examination of charge transfer controlled cathodic currents showed that the direct reduction of carbonic acid is insignificant at the condition of the present study. Additionally, the iron dissolution reaction was found to be significantly affected by the presence of CO$_2$, particularly over the transition and pre-passivation ranges. A comprehensive mathematical model based on the presented mechanistic understanding of the system was developed and used for further quantitative examinations. The present mechanistic model was shown to be able to represent the main mechanistic features of polarization curves and predict the corrosion rates with reasonable accuracy.

The mechanistic understanding of CO$_2$ corrosion, as it relates to that observed in the oil and gas production and transmission facilities, has been evolving significantly over the last 50 years. Amongst numerous studies, a few can be identified as milestones that contributed significantly to our understanding of this process. The well-known studies by de Waard and Milliams are amongst the earliest that addressed the significance of CO$_2$ in acidic corrosion of pipeline steel.[1,2] In those studies, the authors attempted to provide a mechanistic explanation of corrosion in the presence of aqueous CO$_2$, suggesting that the corrosion in CO$_2$-saturated brines is defined mainly by the rate of carbonic acid (H$_2$CO$_3$) reduction as the predominant corrosive species. The authors also introduced their renowned model for prediction of corrosion rate, which gained general acceptance and is still in use to date.[1,2] Considering the current understanding of CO$_2$ corrosion, the mechanism and the model introduced by de Waard and Milliams suffer from many shortcomings, as discussed elsewhere.[3–5] Nevertheless, the reduction of carbonic acid as proposed by the authors, became the center point of the CO$_2$ corrosion mechanism in the following decades.

The study by Schmitt and Rothmann published in 1977 was a notable development in understanding of CO$_2$ corrosion at the time.[6] With the focus on the limiting current densities, the authors demonstrated the significance of the homogeneous CO$_2$ hydration reaction. It was shown that the limiting current in CO$_2$-saturated acidic solutions consists of three components: mass transfer of H$^+$, mass transfer of H$_2$CO$_3$, and kinetically controlled CO$_2$ hydration reaction. The CO$_2$ hydration reaction is indeed a key process that distinguishes the CO$_2$ corrosion from corrosion in strong acid solution or corrosion in presence of other weak acids, such as organic acids and aqueous hydrogen sulfide.

The first mechanistic model of CO$_2$ corrosion was introduced by Gray et al. in 1989.[7] The significance of this study was mainly owed to development of a corrosion rate model using mechanistic description of the underlying electrochemical processes. Additionally, the effect of flow and CO$_2$ hydration reaction were incorporated in the rate calculations. This study demonstrates how the proposed mechanism of CO$_2$ corrosion could quantify the observed electrochemical and corrosion rate behavior. The established mechanism of CO$_2$ corrosion in this study has been widely accepted ever since. In this mechanism, iron dissolution is the main anodic reaction, and the reduction of H$^+$ and

H$_2$CO$_3$ are the two main cathodic reactions, where the concentration of H$_2$CO$_3$ at the surface is buffered by the CO$_2$ hydration reaction.

Nevertheless, it was only after the introduction of more comprehensive mathematical models[8–11] that the true significance of the homogeneous chemical reactions was understood. In these calculations, the kinetics of the homogeneous chemical reactions in an aqueous CO$_2$ solution was coupled with the electrochemical kinetics of the corrosion process. These models demonstrated the significance of the homogeneous H$_2$CO$_3$ and HCO$_3$$^-$ dissociation reactions. It was shown quantitatively that the cathodic limiting currents could be adequately explained even if H$_2$CO$_3$ was not considered an electroactive species.[8–10] This was explained by the homogeneous dissociation of H$_2$CO$_3$ inside the diffusion boundary layer, followed by the reduction of H$^+$ that provides a parallel reaction pathway to the direct reduction of H$_2$CO$_3$; the process that is now commonly referred to as "buffering effect" mechanism. While significant, this mechanistic observation gained little attention until more recent years.[12–15] In fact, this observation undermines the conventional CO$_2$ corrosion mechanism developed based on the earlier works such as those of de Waard and Milliams,[1,2] Schmitt and Rothmann,[6] and Gray et al.[7,16] The arguments in these studies were all based on the analysis of cathodic polarization behavior at or close to limiting currents, where the kinetics of charge transfer reactions could not be properly observed.

In more recent years, the role of H$_2$CO$_3$ has been further investigated. The two possible mechanisms are distinguished as: "direct reduction mechanism" which is based on the assumption that H$_2$CO$_3$ is an electrochemically active species that is reduced during the corrosion process, and the so-called "buffering effect mechanism" that stresses the importance of homogeneous dissociation of H$_2$CO$_3$. It is important to notice that the two roles of H$_2$CO$_3$ (as a buffer and as an electroactive species) are not mutually exclusive, as they are two inherently different, and independent processes.

Being a weak acid, H$_2$CO$_3$ only partially dissociates in an aqueous solution. Therefore, at limiting current conditions when the surface pH is increased, the equilibrium shifts toward dissociation in order to balance ("buffer") the H$^+$ ion concentration. This process results in an increased limiting current as was observed for other weak acids such as acetic acid.[17–19] The extent of this buffering ability is defined by the kinetics and the equilibrium of an individual weak acid. For the case of H$_2$CO$_3$, the relatively low equilibrium constant (pK$_a$ = 3.5 as discussed in section The solution speciation) and the fast kinetics of dissociation (k = 10^8 s^{-1} as discussed in section The solution speciation) suggest that nearly all of H$_2$CO$_3$ could dissociate at limiting current conditions. Independently,

*Electrochemical Society Member.
zE-mail: ak702711@ohio.edu

H_2CO_3 could also be electrochemically active and be reduced at the metal surface, just as the direct reduction mechanism assumes.

Considering the discussion above, the buffering ability arising from the presence of H_2CO_3 as a weak acid is definite. The mechanistic question to be addressed in the present study is whether H_2CO_3 is also electrochemically active or not. The experimental difficulty in examination of this aspect is stemming from the relatively low equilibrium constant of H_2CO_3 and its corresponding fast reaction kinetics, which results in H_2CO_3 readily dissociating as the surface concentration of H^+ decreases. Hence, the current density response of the system is nearly identical under mass transfer limiting conditions, irrespective of whether H_2CO_3 is electrochemically active or not, as noted in the previous studies.[3,8–10,20] The electrochemical activity of H_2CO_3 can only be reasonably discussed by investigating the pure charge transfer controlled cathodic current densities.[3,13,19,20] That is, if H_2CO_3 was a significant electroactive species, the charge transfer controlled currents would increase with increasing H_2CO_3 concentration (which corresponds to increasing CO_2 partial pressure) while the rate of H^+ reduction remains unchanged due to a fixed pH. On the other hand, if the charge transfer controlled currents do not respond to increased CO_2 partial pressure (pCO_2), it can be concluded that the rate of H_2CO_3 reduction is insignificant when compared to the rate of H^+ reduction. Although, this simple hypothesis can be proven with straightforward electrochemical measurement techniques, the main obstacle is creating the conditions where the pure charge transfer controlled current can be observed clearly.

The electrochemical activity of H_2CO_3 on mild steel surface has been the subject of a few studies in more recent years as discussed in more detail in our previous publication.[14] In a study by Linter and Burstein,[21] the charge transfer controlled currents at pH 4 in N_2 and CO_2-saturated solutions were observed by the aid of additional potassium hydrogen phthalate buffer. The addition of this buffer increased the cathodic limiting current density, which allowed the charge transfer controlled currents to be observed. The authors noted that no significant shift in this range of cathodic currents was observed and concluded that H_2CO_3 is not electrochemically active. Later in 2008, Remita et al.[12] used a comprehensive mathematical model to quantify the cathodic polarization curves obtained at pH 4 and 1 bar CO_2 without including H_2CO_3 as an electroactive species. Considering that the polarization curves were reasonably predicted by their model, the authors concluded that H_2CO_3 is not electrochemically active. Nevertheless, in both of the abovementioned studies[12,21] the limited range of the experimental conditions (pH 4 and 1 bar CO_2) makes the generalization of the observed behavior dubious. At pH 4 and 1 bar CO_2, the cathodic currents are dominated by H^+ reduction and the H_2CO_3 concentration is only a fraction of the H^+ concentration (see for example the speciation calculation shown in Figure 8). Hence, even if H_2CO_3 is electrochemically active, its contribution to the overall cathodic current is expected to be small and may not be readily distinguished given the typical experimental error for this type of measurements. This can be also observed in the previous studies,[8,22] where even the models developed based on the direct reduction of H_2CO_3 suggest a very small contribution from this reaction to the net cathodic current at such conditions.

In order to address such deficiencies, Kahyarian et al.[14] investigated the electrochemical activity of H_2CO_3 on X65 mild steel surfaces at pH 4 and CO_2 partial pressures up to 5 bar. In that study, a thin channel flow cell test apparatus was used that allowed experiments to be conducted under a high flow velocity. The increased limiting current, under high flow velocity conditions, allowed the charge transfer controlled currents to be observed clearly, particularly in the experiments conducted at lower temperatures. This range of current densities was found to be independent from the pCO_2 as it was increased from 0 to 5 bar. Therefore, the authors concluded that the direct reduction of H_2CO_3 on a mild steel surface was insignificant in the conditions covered in that study.

Over the past few decades of research, most of the effort was dedicated to clarifying the effect of CO_2 on cathodic currents, while
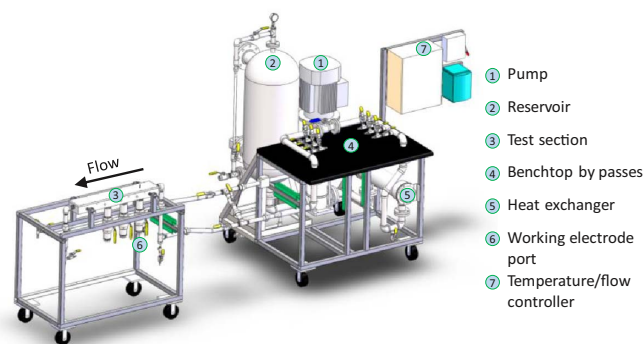

Figure 1. The schematics of the thin channel flow test apparatus.

the effect of CO_2 on the anodic reaction has gained little attention. Nevertheless, a significant change in the behavior of the anodic iron dissolution reaction in the presence of CO_2 has been reported in a few studies. In the study by Linter and Burstein,[21] the authors reported that in CO_2-saturated solutions the rate of iron dissolution from a low alloyed steel is significantly increased in transition and pre-passivation ranges. In another study by Nesic et al.,[23] the authors reported a linear increase of the anodic exchange current densities with pCO_2. This effect was found to reach its maximum as pCO_2 approached 1 bar. The authors hypothesized that the carbonate species enhance the rate of iron dissolution by forming a chemical ligand with the intermediate hydroxides involved in iron dissolution. In a more recent study, Kahyarian et al.[24] further examined the anodic polarization behavior of X65 mild steel in mildly acidic solutions saturated at elevated CO_2 partial pressures (up to 5 bar). A significant influence of CO_2 on the iron dissolution in the transition and pre-passivation ranges was also reported in that study,[24] in agreement with what was suggested by Linter and Burstein.[21] The authors also noted that the reaction rates in the active dissolution range of the anodic polarization curves were slightly increased with the introduction of CO_2, while that effect was not further intensified as the pCO_2 was increased from 1 bar to 5 bar. The latter also appeared to be, to some extent, in agreement with what was suggested by Nesic et al.[23]

As it appears from the short review of the literature presented herein, the mechanistic understanding of CO_2 corrosion has been evolving in the last few years rather significantly. In order to further elucidate the mechanism of the CO_2 corrosion, the present investigation expands on our earlier studies[14,24] by extending the range of experimental conditions, and also, by introducing a comprehensive mathematical model based on the latest mechanistic observations. This combined approach allowed for a comprehensive quantitative examination of the proposed mechanisms, when it comes to the electrochemical activity of H_2CO_3 and the effect of CO_2 on the iron dissolution reaction. Additionally, the ability of the model for corrosion rate prediction based on the recently understood mechanisms was evaluated.

Methodology

The experiments were conducted in a thin-channel flow cell (TCFC) test apparatus shown in Figure 1. This test apparatus consists of a 200 L reservoir, a high power centrifugal pump, a heat exchanger, the thin channel test section, and a set of bypasses that allow pH measurement and adjustment. All the components of this experimental apparatus are made of 316L stainless steel.

The thin channel test section has an interior height of $\sim$3.57 mm (9/64 inch) and width of 8.89 cm (3.5 inch), creating fully developed, well-defined one-dimensional flow field at the locations where electrodes are placed. The electrochemical measurements were done using a three-electrode arrangement with the cell body serving as the counter electrode, and an in-house built silver/silver chloride reference electrode, as shown in Figure 2. The reference electrode was checked for
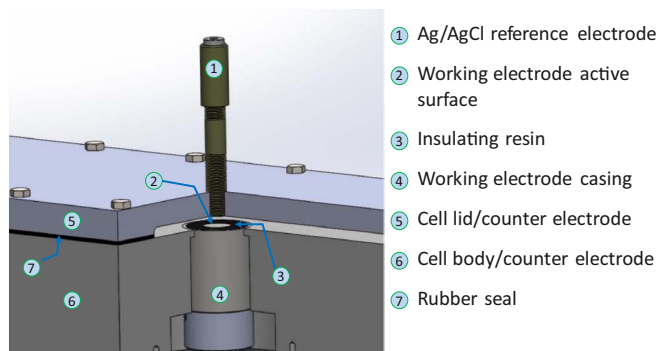
Figure 2. The schematics of the electrode arrangement inside the thin channel flow cell.

its performance prior to each test using a saturated calomel electrode (-45 ± 5 mV). The minor deviations were accounted for when polarization data were shifted to standard hydrogen electrode reference for quantitative analysis. The flow velocity inside the test section was maintained at 12.9 m.s^{-1} in all the experiments by fixing the pump output to ~4.1 L.s^{-1} (65.0 ± 0.5 gal.min^{-1}).

The experiments were conducted using 0.1 M NaCl supporting electrolyte (110 L) made of deionized water and analytical grade chemicals. The solution was de-oxygenated prior to each test using CO_2 or N_2 gas for at least 2 hr, depending on the experiments. Meanwhile, the oxygen content of the solution was monitored using an in-line Orbisphere 410 oxygen sensor. The de-oxygenation step was continued until the dissolved oxygen concentration was reduced to 3 ppb$_m$ level. For high-pressure experiments, this step was followed by pressurizing the system to 5 bar using CO_2 gas. The next step was only performed after the equilibrium at this high pressure was achieved, typically after 5 hr. The constant pH and pCO$_2$ readouts were considered as the criteria for assessing if the equilibrium was achieved. This was followed by pH adjustment, done by injection of de-oxygenated HCl or NaOH solutions from a secondary 0.5 L reservoir connected via a bypass line. The pH was monitored throughout the experiments using an in-line high-pressure pH probe (Omega PHE-3431).

The working electrode assembly (shown in Figure 2) was made of a disk shaped (0.952 mm (3/8 inch) diameter) API 5L X65 mild steel with the chemical composition shown in Table I. The sample was placed inside a 316 L stainless steel casing with an insulation epoxy resin filling the gap in between. Prior to each experiment, the working electrode was abraded using 600 grit silicon carbide paper, rinsed and sonicated in isopropanol alcohol, and dried using N_2 gas. The working electrode was then immediately mounted in the test section. After sealing, the test section was purged using CO_2 or N_2 gas and pressurize up to the working pressure. The solution temperature was controlled within $\pm 0.5°$C by using a jacketed immersion heater located in the tank and covered cartridge heaters to directly heat the test section (for experiments conducted at 30°C) as well as a shell and tube heat exchanger connected to a chiller (Air-3000 FLUID CHILLERS Inc.) for experiments done at 10°C.

After exposing the test section and the electrode to the test solution, the open circuit potential (OCP) was monitored for 20 min to ensure that a steady state value was reached (maximum of ± 2 mV drift over 5 min) prior to initiating polarization measurements. The cathodic and anodic polarization curves were obtained in separate experiments by sweeping the potential from OCP toward more negative and positive values, respectively. The measurements were performed using staircase voltammetry at 0.5 mV.s^{-1} scan rate and 1 s^{-1} sampling period. The reported polarization curves were corrected for ohmic drop with the solution resistance obtained by electrochemical impedance spectroscopy (EIS) measurements (at OCP, AC potential perturbation of 5 mV, frequency range 100kHz to 0.2 Hz at 10 points/dec) performed 15 min after polarization measurements, when a steady OCP was established. The linear polarization measurements were performed

Table I. Chemical composition of the X65 mild steel in wt%.

S	P	V	C	Cr	Mo	Si	Ni	Mn	Fe
0.009	0.009	0.047	0.13	0.25	0.16	0.26	0.29	1.16	Balance

in separate experiments, following the abovementioned preparation procedure. The measurements were done by sweeping the potential from -5 mV to $+5$ mV vs. OCP, using 0.125 mV.s^{-1} scan rate and 1 s^{-1} sampling period. The experimental conditions are summarized in Table II.

Results and Discussion

The TCFC has two main advantages when compared to the conventional glass cell or autoclave experimental setups. First, it allows the experiments to be conducted under high flow velocities with well-defined, and reproducible hydrodynamics. This capability allows the mass transfer limitation to be increased, thus, enhances the ability to investigate the behavior of the charge transfer controlled currents. Second, the TCFC test apparatus used in the present study, allows the experiments to be conducted at up to 5 bar pCO$_2$, enabling the comparison of the charge transfer controlled currents across a broader range of conditions. As discussed above, one of the main challenges of mechanistic investigation of CO_2 corrosion of mild steel is the difficulty in obtaining clear charge transfer controlled polarization data, which in typical glass cell experiments are obscured by the limiting current. The abovementioned advantages of the TCFC, made this test apparatus an appealing choice for the purpose of the present study.

The polarization data obtained on API 5L X65 mild steel surface at pH 4 and pH 5 are shown in Figure 3A and Figure 3B, respectively, where a significant influence of pCO$_2$ was observed on both the cathodic and the anodic current densities. At both pH 4 and pH 5, the cathodic limiting current densities were linearly increasing with respect to pCO$_2$, as expected. However, the charge transfer cathodic current densities displayed two distinct behaviors when comparing the results obtained at pH 4 with those at pH 5.

The cathodic polarization curves at pH 4 (Figure 3A) show a Tafel range just below the OCP that is mostly governed by the charge transfer kinetics (as further examined in model verification section). This range of cathodic current densities was found not to be significantly affected by the pCO$_2$. This behavior is expected when carbonic acid is not significantly electroactive, where increasing its concentration (by increasing pCO$_2$) does not affect the charge transfer cathodic current. The present results were found to be in agreement with what was reported previously by Tran et al. on a stainless steel surface,[13] and also in our earlier study.[25] However, the cathodic currents obtained at pH 5 (Figure 3B) were fully under limiting current control even at pCO$_2$ = 5, which would not allow for corroboration of the mechanistic behavior observed at pH 4.

Over the anodic current range, the polarization curves showed a significant effect of pCO$_2$ on the electrochemical behavior of the iron dissolution reaction. The anodic polarization curves do not show the linear range associated with the active dissolution of iron (as suggested by El Miligy et al.[26]) in any of the conditions tested. The observed behavior is perhaps best categorized as the transition range and pre-passivation range,[26] while the active dissolution range was "hidden" behind the cathodic currents. The transition range, indicated by the local anodic current maximum (or in some cases merely an inflection point), and the pre-passivation range, indicated by the linearly increasing current densities at more positive potentials, were found to be significantly affected as pCO$_2$ was increased. The significance of this effect is best seen in the polarization curves obtained at pH 5. At this condition, the anodic currents increased "hand in hand" with the cathodic limiting current densities. That resulted in the corrosion current remaining under cathodic limiting current control, even though the limiting currents were increased significantly at elevated pCO$_2$.
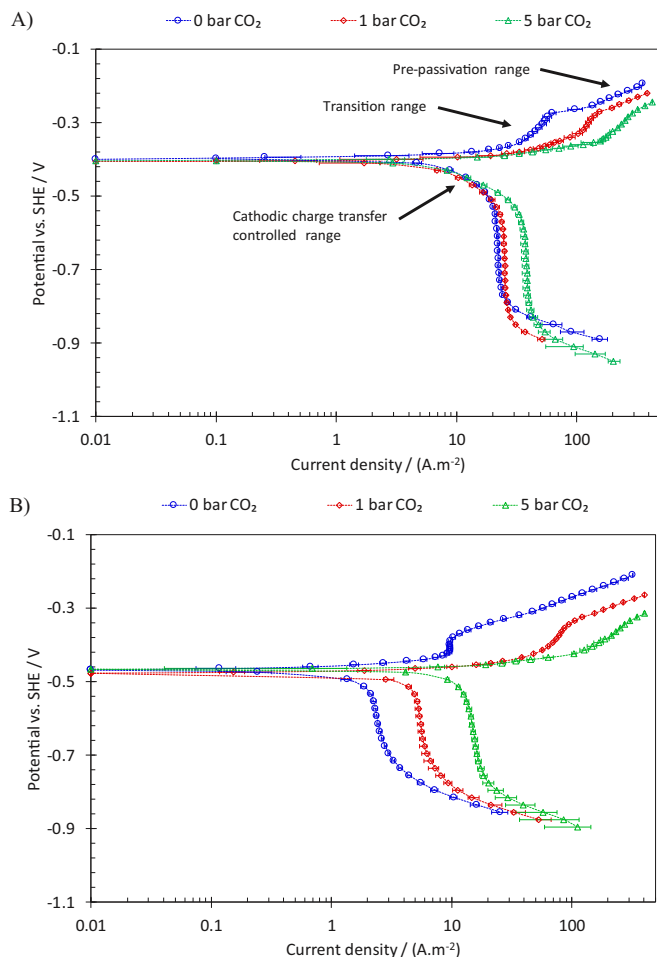
Figure 3. The anodic and cathodic polarization behavior of API 5L X65 mild steel in acidic solutions, at 30°C, 12.9 m.s^{-1} flow velocity, 0.1 M NaCl, and varying pCO$_2$. A) at pH 4. B) at pH 5. Error bars represent the standard deviation of at least three repeated experiments at selected potentials.

Figure 4. The measured corrosion rates on API 5L X65 mild steel in acidic solutions, at 30°C, 12.9 m.s^{-1} flow velocity, 0.1 M NaCl, and varying pH and pCO$_2$. Error bars represent the standard deviation of at least five repeated measurements.

of the passive layer, Fe(OH)$_2$ or Fe$_2$O$_3$ species, through a chemical attack by bicarbonate ion, similar to that proposed for the alkaline pH range.[27–29] Nevertheless, such a hypothesis cannot be introduced for the conditions of the present study, considering that the formation of passive layers on a mild steel surface is not thermodynamically favored in the pH and potential range used here.[30]

The effect of pCO$_2$ on the corrosion rates is examined based on the experimental data from LPR measurements as summarized in Table III. The resistance obtained from LPR measurement was first corrected for solution resistance (from EIS measurements) to obtain the polarization resistance (R_p). The polarization resistance was then used to obtain the corrosion rate based on the Stern-Geary relationship, Equation 1, where A is the electrode surface area (m^2), and 1.16 is the proportionality constant for converting the corrosion current (A.m^{-2}) to corrosion rate (mm.yr^{-1}) of steel. The proportionality constant, B in Equation 2, was estimated based on apparent anodic and cathodic charge Tafel slopes (b_a and b_c, respectively) as observed in polarization data corresponding to each condition (shown in Figure 3 and Figure 6).

$$CR = 1.16 \frac{B}{R_p/A} \qquad [1]$$

$$B = \frac{b_a b_c}{2.303 (b_a + b_c)} \qquad [2]$$

The effect of pCO$_2$ on corrosion rates at pH 4 and pH 5 is shown in Figure 4. The general trend of corrosion rate vs. pCO$_2$ was found to agree well with the mechanistic discussion above. At pH 4, the cathodic currents were under charge transfer control, hence, corrosion rates show only a slight increase as pCO$_2$ was increased from 0 to 5 bar. The slight increase of corrosion rates could be explained by

The effect of CO$_2$ on the iron dissolution reaction is perhaps one of the least studied aspects of CO$_2$ corrosion. Even in the few available studies a rather inconsistent behavior was reported as discussed in more detail elsewhere.[24] The significant increase of the anodic reaction rate in the transition and pre-passivation ranges as shown in Figure 3, appears to be in agreement with the results reported previously by Linter and Burstein.[21] In that study, the authors suggested that the increased rate of iron dissolution was a result of the destabilization
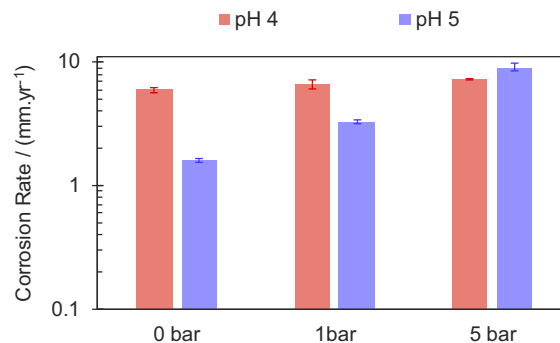
Table II. Summary of experimental conditions.

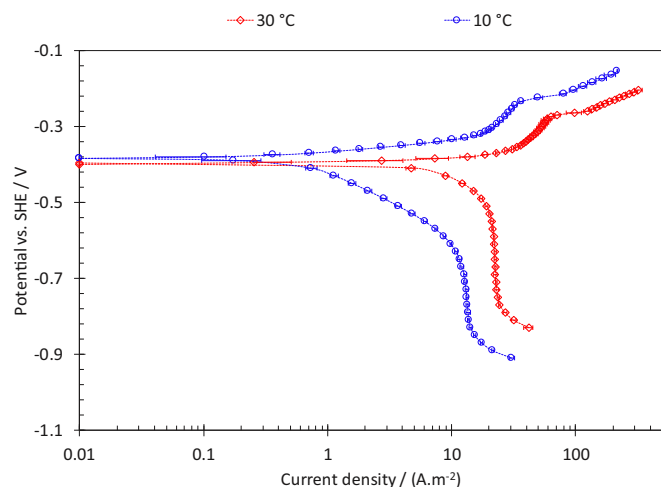| Test Apparatus					TCFC
Electrode material					API 5L X65
Electrode Surface Area (m^2)					1.99×10^{-4}
Flow Velocity (m.s^{-1})					12.9
Channel hydrodynamic length (m)					6.9×10^{-3}
Temperature (°C)					30, 10
pH					4.0, 5.0
Gas composition	Temperature (°C)	Total Pressure (bar)	pH$_2$O (bar)	pN$_2$ (bar)	pCO$_2$ (bar)
	10	1	0.012	Balance	0
	10	1	0.012	0	Balance
	10	5	0.012	0	Balance
	30	1	0.043	Balance	0
	30	1	0.043	0	Balance
	30	5	0.043	0	Balance

Figure 5. The effect of temperature on the observed polarization behavior of API 5L X65 mild steel in N_2-saturated acidic solutions at pH 4, 12.9 m.s^{-1} flow velocity, 0.1 M NaCl. Error bars represent the standard deviation of at least three repeated experiments at selected potentials.

the influence of CO_2 on the anodic reaction. On the other hand, at pH 5 corrosion rates were significantly influenced by pCO_2, where almost a five-fold increase was observed by increasing the pCO_2 from 0 to 5 bar. The polarization curves obtained at the similar conditions (Figure 3B), showed that corrosion was controlled by the cathodic limiting currents at all CO_2 partial pressures. Hence, the increased corrosion rates are the result of increased cathodic limiting currents, and to a smaller extent due to the increased rate of the anodic reaction.

In our further attempts to corroborate the mechanistic arguments above, a set of experiments at a lower temperature (10°C) were conducted in the present study. Decreasing the temperature was expected to influence the observed polarization curves by disproportionally decreasing the rate of charge transfer reactions as compared to the limiting current. Such behavior would allow the charge transfer cathodic currents and the anodic currents in the active dissolution range to be observed more clearly, hence giving us a better chance to refine these mechanistic arguments.

The polarization data obtained on X65 mild steel under N_2 atmosphere at pH 4 and 10°C is compared with those obtained at 30°C, and shown in Figure 5. The results were in agreement with the expected behavior, where at 10°C a clear Tafel behavior observed over the cathodic currents, indicating a charge transfer controlled range. Moreover, the anodic current densities exhibit a linear range just above the OCP, which corresponds to the active iron dissolution range. The clear separation between the cathodic and anodic currents observed at this lower temperature provides a great opportunity for better understanding of the effect of CO_2 on the electrochemical behavior of this system.

The effect of pCO_2 on the observed polarization behavior at pH 4 and pH 5 was re-examined at 10°C, as shown in Figure 6. At pH 4, the charge transfer controlled cathodic currents were observed clearly over an extended potential range. The behavior of cathodic currents with pCO_2 was in complete agreement with that observed at 30°C in Figure 3A. The experimental data obtained at pH 5 also showed a similar range of charge transfer controlled current densities that was not significantly affected by increasing the pCO_2 from 1 to 5 bar. This observation further corroborates the abovementioned mechanistic arguments that carbonic acid is not a significant electroactive species even if at pH 5 and 5 bar CO_2 the concentration of carbonic acid was about 40 times higher than that of H$^+$.

The anodic polarization curves obtained at 10°C clearly demonstrate a range of linearly increasing anodic currents associated with the active dissolution range, in addition to the transition and pre-passivation ranges. The electrochemical behavior in the transition and
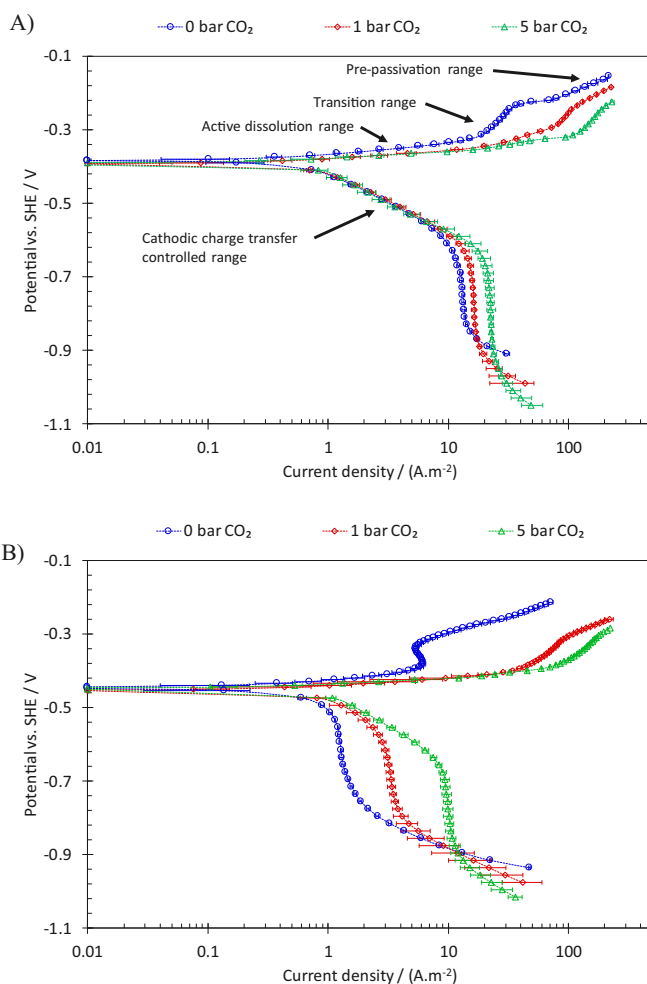

Figure 6. The anodic and cathodic polarization behavior of API 5L X65 mild steel in acidic solutions, at 10°C, 12.9 m.s^{-1} flow velocity, 0.1 M NaCl, and varying pCO_2. A) at pH 4. B) at pH 5. Error bars represent the standard deviation of at least three repeated experiments at selected potentials.

the pre-passivation range were similar to that observed at 30°C. In the active dissolution range, the presence of CO_2 led to observation of a slightly decreased Tafel slope, when comparing to the polarization curves obtained without CO_2 at the same pH. This decrease of the Tafel slope was not intensified at higher CO_2 partial pressures. The observed influence of CO_2 on anodic reaction in the active dissolution range was found to partially agree with the results reported by Nesic et al.[23] In that study[23] the authors investigated the effect of CO_2 on the anodic polarization curves in a narrow potential range (~100 mV) above the corrosion potential. The proposed mechanism by Nesic et al.[23] suggests that CO_2 is actively engaged in the electrochemistry of iron dissolution. The trend in the present study also suggest that the presence of CO_2 resulted in an increased rate in the active dissolution range, which was not further intensified as pCO_2 was increased from 1 bar to 5 bar. However, here the effect appears to be in the form of a slight decrease in the apparent Tafel slope.

The corrosion rates obtained for pH 4 and pH 5 at 10°C based on LPR measurements, are shown in Figure 7. These values are generally about three times smaller than those obtained at 30°C. The corrosion rates reported here show only a small dependence on pCO_2. As is clearly observed in the polarization curves in Figure 6, at 10°C the cathodic currents are under charge transfer control, hence increasing pCO_2 does not result in higher cathodic currents, as expected based on the mechanistic arguments above. Additionally, the anodic reaction in the vicinity of OCP was in the active dissolution range, which was only
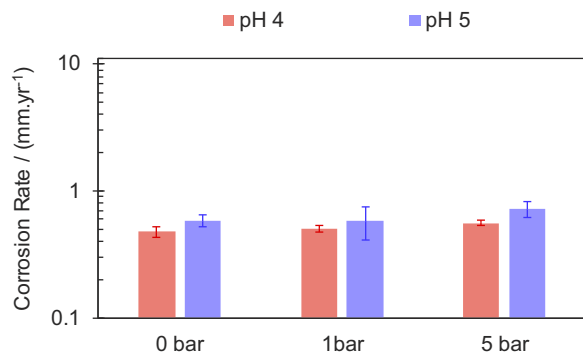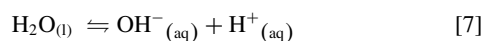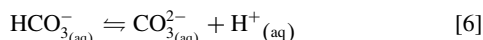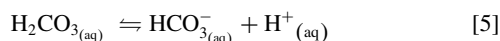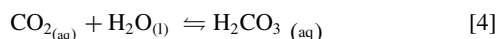
Figure 7. The measured corrosion rates on API 5L X65 mild steel in acidic solutions, at 10°C, 12.9 m.s^{-1} flow velocity, 0.1 M NaCl, and varying pH and pCO$_2$. Error bars represent the standard deviation of at least five repeated measurements.

slightly affected by pCO$_2$. Considering these mechanistic behaviors, the observed trend of corrosion rates vs. pCO$_2$ in Figure 7 was found to be consistent with what was expected. Unlike what was observed at 30°C for pH 5, at 10°C the corrosion rates were found to be mostly insensitive to pCO$_2$.

Quantitative Analysis

The solution speciation.—The calculation of the solution composition is a primary step in mathematical modeling of CO$_2$ corrosion. The primary objective in such calculations is to determine the solution speciation as it is dictated by the equilibria associated with H$_2$O/CO$_2$ system. That includes the CO$_2$ dissolution, hydration and dissociation reactions as well as water dissociation as shown by Reactions 3 through 7.

$$CO_{2(g)} \leftrightharpoons CO_{2(aq)} \qquad [3]$$

$$CO_{2(aq)} + H_2O_{(l)} \leftrightharpoons H_2CO_{3\ (aq)} \qquad [4]$$

$$H_2CO_{3(aq)} \leftrightharpoons HCO_{3(aq)}^- + H^+_{(aq)} \qquad [5]$$

$$HCO_{3(aq)}^- \leftrightharpoons CO_{3(aq)}^{2-} + H^+_{(aq)} \qquad [6]$$

$$H_2O_{(l)} \leftrightharpoons OH^-_{(aq)} + H^+_{(aq)} \qquad [7]$$

In a generic formulation, the aqueous chemical equilibrium for any reaction j, with n_r reactants (R_m) and n_p products (P_n), in the form of:

$$\sum_{m=1}^{n_r} R_m \rightleftharpoons \sum_{n=1}^{n_p} P_n \qquad [8]$$

is expressed as Equation 9, assuming an ideal solution conditions:

$$\frac{\prod_{n=1}^{n_p} c_{P_n}}{\prod_{m=1}^{n_r} c_{R_m}} = \frac{k_{f,j}}{k_{b,j}} = K_j \qquad [9]$$
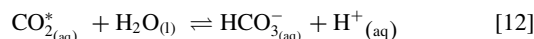
where c_i is the concentration of the chemical species i (M or m depending on corresponding K_j units), K_j is the equilibrium constant of reaction j, and $k_{f,j}$ and $k_{b,j}$ are the kinetic rate constants associated with the forward and backward reactions involved in each equilibrium.

The phase equilibrium of CO$_2$ dissolution in water (Reaction 3) can be expressed based on Henry's law, assuming an ideal solution:

$$\frac{\varphi_{CO_2} p_{CO_2}}{c_{CO_2}} = H_{CO_2} \qquad [10]$$

where ϕ_{CO2} and p_{CO2} (bar) are fugacity coefficient and partial pressure of CO$_2$, respectively, and H_{CO2} is the Henry's constant. The fugacity coefficient of CO$_2$ can be obtained using the empirical equations reported by Duan et al.[31] as shown in Table IV. In the conditions of this study the partial pressure of CO$_2$ in the gas phase is $P_{CO_2} = P_{tot} - P_{ws}$, with P_{tot} (bar) being the total pressure of the system and P_{ws} being the saturation pressure of water that was obtained from the empirical relationship shown in Table III.

In the literature dedicated to the equilibrium and speciation of a H$_2$O/CO$_2$ system, it is customary to lump the concentration of the dissolved CO$_2$ with carbonic acid to define $C_{CO_{2(aq)}^*} = C_{CO_{2(aq)}} + C_{H_2CO_{3(aq)}}$. Therefore, the equilibria are commonly discussed in terms of Reaction 11 and Reaction 12, where carbonic acid is not considered explicitly.

$$CO_{2(g)} \rightleftharpoons CO_{2(aq)}^* \qquad [11]$$

$$CO_{2(aq)}^* + H_2O_{(l)} \rightleftharpoons HCO_{3(aq)}^- + H^+_{(aq)} \qquad [12]$$

The corresponding equilibrium constants (denoted by asterisk) are therefore reported as:

$$H_{CO_2^*}^* = \frac{\varphi_{CO_2} p_{CO_2}}{c_{CO_2^*}} \qquad [13]$$

$$K_{Ca}^* = \frac{c_{HCO_{3(aq)}^-} c_{H^+(aq)}}{c_{CO_{2(aq)}^*}} \qquad [14]$$

The effect of the hydration reaction can be readily included in these expressions in order to obtain the true equilibrium constants, required for the water chemistry calculation in the CO$_2$ corrosion context. The relationship between the K^* values and the true equilibrium constants can be obtained by simple mathematical manipulations:

$$H_{CO_2} = \left(1 + K_{hyd}\right) H_{CO_2^*}^* \qquad [15]$$

$$K_{Ca} = \left(1 + \frac{1}{K_{hyd}}\right) K_{Ca}^* \qquad [16]$$

The Henry's constant as well as the equilibrium constants for carbonic acid (K_{Ca}), bicarbonate ion (K_{bi}) and water dissociation (K_w) reactions are listed in Table IV.

The equilibrium constant for CO$_2$ hydration (Reaction 4), K_{hyd}, is perhaps the constant that is known with the least confidence. There have been a number of different studies dedicated to evaluation of this parameter.[32–37] The earlier attempts have been reviewed by Kern[33] and were shown to be scattered over a rather wide range. The commonly used value of $K_{hyd} = 2.58 \times 10^{-3}$ is in fact at the higher end of the reported range.[8,38,39] The reason could be that it was evaluated based on the value of $pK_{Ca} = 3.76$ (see Equation 12) reported by Wissbrun in 1954.[40] The recent studies[35,41,42] suggest that the pK_{Ca} range (3.40–3.50) is significantly lower than that reported by Wissbrun.[40] The discrepancies of reported pK_{Ca} values, and hence the K_{hyd}, are mostly due to the strong influence of solution non-idealities, in addition to the inherent measurement uncertainties. However, the K_{hyd} can also be obtained from the forward and backward kinetic rate constants of the hydration reaction. Since this reaction only involves neutral species, the effect of non-ideal solution is minimal; hence, the reported values are in that sense more reliable. With these considerations in mind, the relationship based on a kinetic model by Wang et al.[37] (shown in Table IV) was used in the present study.

In addition to the equilibrium relationships of the H$_2$O/CO$_2$ system, the concentration of ions must also satisfy the charge balance as shown by Equation 17.

$$\sum_i z_i C_i = 0 \qquad [17]$$

In the present study, where the pH and the pCO$_2$ are known, solution speciation can be obtained from the relationships describing the chemical equilibria, and the electro-neutrality equation. This

Table III. Summary of polarization resistance and solution resistance data based on LPR and EIS measurements, respectively, used for corrosion rate calculation.

Temperature (°C)	pH	pCO2 (bar)	data points #	Polarization resistance (Ω)		Solution resistance (Ω)		B Value	Corrosion rate (mm.yr^{-1})	
				Average value	Standard deviation	Average Value	Standard deviation		Average value	Standard deviation
30	4.0	0	7	16.8	0.5	5.8	0.2	0.011	5.97	0.27
30	4.0	1	10	15.6	2.0	5.1	0.5	0.011	6.66	0.57
30	4.0	5	9	13.1	0.4	5.4	0.3	0.010	7.26	0.48
30	5.0	0	8	52.6	3.6	5.5	0.6	0.013	1.62	0.12
30	5.0	1	8	22.5	0.8	4.9	0.5	0.010	3.31	0.11
30	5.0	5	7	11.5	0.7	5.4	0.5	0.010	9.14	0.73
10	4.0	0	5	125.3	16.6	7.4	0.5	0.010	0.48	0.04
10	4.0	1	5	99.9	7.8	7.6	0.3	0.011	0.51	0.03
10	4.0	5	4	87.0	11.5	8.3	0.4	0.010	0.56	0.03
10	5.0	0	6	140.8	11.1	7.9	0.4	0.010	0.58	0.06
10	5.0	1	11	96.7	24.4	7.8	0.5	0.008	0.58	0.17
10	5.0	5	12	76.0	10.7	8.0	0.3	0.008	0.72	0.10

set of equations can be expressed in a matrix format in the form of Equation 18, so that the solution speciation can be directly obtained by calculating the inverse of the coefficient matrix [A] (Equation 19).

$$[A] \cdot [C] = [S] \quad\quad [18]$$

$$[C] = [A]^{-1} \cdot [S] \quad\quad [19]$$

An example of one such calculation is shown by Equation 20, which, includes NaCl as well as NaOH concentrations. The latter being the required concentration of NaOH to adjust the pH to the pre-specified value. Figure 8 illustrates the solution speciation as a function of pH for an open system at 1 bar and 5 bar pCO2, obtained following this procedure.

$$
\begin{bmatrix}
1 & 0 & 0 & 0 & 0 & 0 & 0 & 0 & 0 & 0 \\
0 & 0 & 1 & 0 & 0 & 0 & 0 & 0 & 0 & 0 \\
1 & -K_{H,CO_2} & 0 & 0 & 0 & 0 & 0 & 0 & 0 & 0 \\
0 & -K_{hyd} & 0 & 1 & 0 & 0 & 0 & 0 & 0 & 0 \\
0 & 0 & 0 & -K_{ca} & 10^{-pH} & 0 & 0 & 0 & 0 & 0 \\
0 & 0 & 0 & 0 & -K_{bi} & 10^{-pH} & 0 & 0 & 0 & 0 \\
0 & 0 & 0 & 0 & 0 & 0 & 10^{-pH} & 0 & 0 & 0 \\
0 & 0 & 1 & 0 & -1 & -2 & -1 & -1 & 1 & 0 \\
0 & 0 & 0 & 0 & 0 & 0 & 0 & 1 & 0 & 0 \\
0 & 0 & 0 & 0 & 0 & 0 & 0 & 0 & 1 & -1
\end{bmatrix}
$$

$$
\cdot
\begin{bmatrix}
f_{CO_2} \\
c_{CO_{2(aq)}} \\
c_{H^+{}_{(aq)}} \\
c_{H_2CO_{3(aq)}} \\
c_{HCO_3^-{}_{(aq)}} \\
c_{CO_3^{2-}{}_{(aq)}} \\
c_{OH^-{}_{(aq)}} \\
c_{Cl^-{}_{(aq)}} \\
c_{Na^+{}_{(aq)}} \\
c_{NaOH_{(aq)}}
\end{bmatrix}
=
\begin{bmatrix}
p_{CO_2}\phi_{CO_2} \\
10^{-pH} \\
0 \\
0 \\
0 \\
0 \\
a_{H_2O}\,K_w \\
0 \\
c_{NaCl_{(aq)}} \\
c_{NaCl_{(aq)}}
\end{bmatrix}
\quad [20]
$$

The electrochemical reactions.—The mathematical model presented below is a quantitative attempt to validate the experimental findings, and ultimately to use the current mechanistic understanding of CO2 corrosion for predicting the corrosion rates. Hence, the carbonic acid reduction reaction as proposed in the conventional mechanism of CO2 corrosion is not included in the present model. Also, the water reduction reaction that is only occurs significant at notably lower potentials, was not included in the model. Therefore, the present model is developed with H$^+$ as the sole cathodic reaction and iron dis-

solution as the only anodic reaction as shown via Reactions 21 and 22. It should be noted that due to the negligible concentration of dissolved H2 gas and the potential range of interest in these applications, the H2 oxidation reaction can be assumed to be insignificant. Similarly, considering the negligibly small concentration of ferrous ion in the
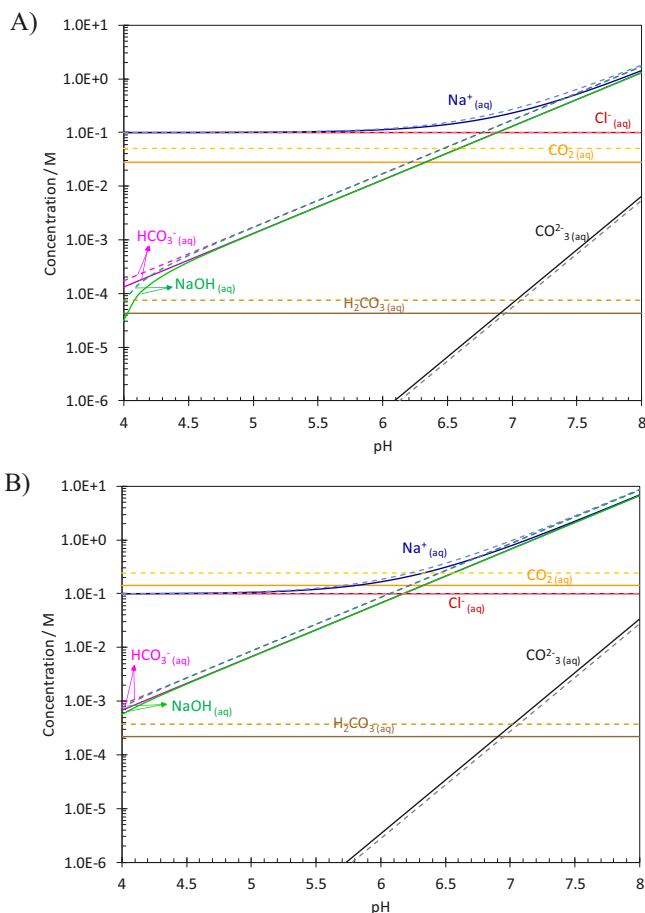

Figure 8. The pH dependence of carbonate speciation at 1 bar CO2 (solid lines) and 5 bar CO2 (dashed lines), at A) 30°C. B) 10°C. The concentration of the alkalinity required at any pH value is included in the form of NaOH.

present study, the iron reduction reaction was omitted.

$$H^+ + e^- \rightarrow \frac{1}{2}H_2 \qquad [21]$$

$$Fe \rightarrow Fe^{2+} + 2e^- \qquad [22]$$

The rate of the H^+ reduction reaction is expressed as shown by Equation 23, where k_{H^+}, m_{H^+}, and α_{H^+} are the reaction rate constant, reaction order, and charge transfer coefficient, respectively, which are estimated based on the experimental data as further discussed below. The current density calculations are based on the surface concentration of the active species denoted by $C_{H^+}^s$ in the case of H^+ reduction reaction. It is worthwhile to note that the potential dependence in Equation 23 is expressed in terms of applied potential (E_{app}), and the standard potential term as a constant value parameter in the exponent, is lumped into the rate constant.

$$i_{c,H^+} = -n_{H^+}Fk_{H^+}C_{H^+}^{s\ m_{H^+}}e^{\left(\frac{-\alpha_{H^+}FE_{app}}{RT}\right)} \qquad [23]$$

The iron dissolution reaction in acidic solutions can be considered as one of the classic subjects in electrochemical mechanism studies, which has been extensively studied over the last decades.[26,43–50] An extensive review of the literature is beyond the scope of this study; however, the interested readers can find a wealth of information in the reviews dedicated to this subject.[51,52] In the classical view, the iron dissolution was believed to occur either through the so-called "catalytic mechanism" or "consecutive mechanism", depending on the surface activity and microstructure of the metal substrate.[46,47,49,51–53] Further mechanistic studies suggest that the iron dissolution occurs through a series of parallel reactions, and depending on the rate determining step, the observed behavior can be associated with either of the previously proposed mechanisms.[50,52,54] The more recent studies also provide further mechanistic insight into the transition and the pre-passivation ranges of the iron dissolution reaction, suggesting that the active dissolution range is followed by higher order surface oxidation of the iron intermediates.[49,50,52,54]

Despite the advancements in the understanding of the iron dissolution mechanism, its inherent complexity has left some mechanistic aspects of this reaction controversial, more specifically when it comes to the interpretation of the observed behavior in terms of electrochemical steps. While it has been shown that the models based on the uniform surface chemistry mechanisms[47] are not able to reasonably explain the observed EIS measurements,[50,51,54] the proposed alternative, the self-catalytic two-electron transfer step of the "catalytic mechanism", has also been criticized.[47] This latter reaction is suggested to occur on self-reproducing "kink" sites.[43,51] However, the nature of the kink sites, and quantitative measures of their potential and pH dependence, which are of great significance in determining the reaction rate, requires further elucidation. In a more recent publication, Lorenz et al.[49] offered some alternative explanation in this regards, which are based on the surface morphology and the low dimension systems concept.

Aside from these lingering controversies, considering the inherent complexity of the iron dissolution reaction with numerous elementary steps and intermediate species, a fully mechanistic, micro-kinetic mathematical description of this process is a significant undertaking, that is beyond the scope of the corrosion rate predictive model considered in the present study. Additionally, the effect of the solution composition and the presence of various anions are known to influence not only the kinetics, but also the mechanism of the iron dissolution reaction.[17,48,52,55] On top of that, in the context of CO_2 corrosion, the non-uniform steel surface and more importantly, the lack of understanding of the effect of carbonate species on the mechanism of iron dissolution reaction are amongst the additional complexities.

Despite the abovementioned complications in iron dissolution rate calculations, the rate of this reaction in CO_2-saturated solutions is commonly expressed in terms of a simple elementary electron transfer reaction.[8,22,56,57] That treatment practically assumes that the iron dissolution reaction always occurs in the active dissolution range.

Considering the observed behavior in Figure 3, and also that reported in the previous studies,[23,24,26,50] this is an obvious oversimplification that is not in accord with experimental observations. The experimental data reported in Figure 5 or those in Figure 3B and Figure 6B, suggest that the corrosion current can be either in the active dissolution, transition or pre-passivation range. That is defined by the surface pH, which in addition to bulk pH, is also depends on temperature, pCO_2, etc. Therefore, in corrosion rate predictive models it is critical to include a rate expression that reasonably reflects the behavior of the anodic reaction over all its various ranges.

In an attempt to quantify the observed behavior in the active dissolution, as well as those in the pre-passivation and the transition ranges, the rate of the iron dissolution reaction is expressed using a semi-empirical approach. In this approach while all the major components of the iron dissolution mechanism are accounted for, some details of the underlying mechanism are inevitably disregarded to simplify the rate expression. As a high level explanation, the iron dissolution from the active to the pre-passive range consists of four main processes, which are in common in almost all proposed mechanisms.[48,50–52,58] Those are: two linear ranges in a semi-log plot, one for the active dissolution range and the other for pre-passivation range, the presence of a current maximum in the transition range, and its gradual disappearance with change in solution pH. The linearly increasing current density in the active dissolution range and that in the pre-passivation range were clearly observed in the experimental results shown above in Figure 6. Regardless of the physical explanations, the current/potential relationship in these ranges can be expressed as following, considering the electrochemical nature of their corresponding reactions:

$$i_{a,j} = n_{Fe}Fk_jC_{H^+}^{s\ m_{H^+,j}}e^{\left(\frac{\alpha_jFE_{app}}{RT}\right)} \qquad [24]$$

where $C_{H^+}^s$ is the surface concentration of H^+ to represent the pH dependence of the iron dissolution with the apparent reaction order of $m_{H^+,j}$. It should be noted that Equation 24 does not represent the current/potential dependence of a single elementary reaction, rather it represents the response of a sequence of reactions, and the kinetic parameters are representing the apparent values.

There is an agreement in the literature that the pre-passivation range is a result of the oxidation of an existing intermediate species to higher orders.[49,50,52,54] Such processes commonly exhibit a Tafel slope lower than $2RT/F$ (similar to that observed in the active dissolution range), unless the surface coverage of the intermediate species (θ) is not potential dependent, i.e. when $\theta \rightarrow 1$. The observation of a ~120 mV Tafel slope in the pre-passivation range supports such a scenario. The concentration of this intermediate can be expressed using a Langmuir isotherm for an electrochemical process, Equation 25. Furthermore, such a process suggests that the 120 mV range is only observed when $\theta \rightarrow 1$, where the rate of other electrochemical reactions are inevitably halted due to lack of available reaction sites. Therefore, Equation 25 as the third main component of the anodic polarization curve, is responsible for the "S" shape behavior observed in the transient range. In order to reflect the effect of the intermediate surface species, the rate of all electrochemical reactions are multiplied by $(1-\theta)$, which represents the available sites for those reactions. The consistent observation of this behavior beyond the transition range suggests that the potential and concentration dependences of this passivating process are likely to be similar to those in the active dissolution range.

$$\theta = \frac{K_\theta C_{H^+}^{s\ m_{H^+,\theta}}e^{\left(\frac{\alpha_\theta FE_{app}}{RT}\right)}}{1 + K_\theta C_{H^+}^{s\ m_{H^+,\theta}}e^{\left(\frac{\alpha_\theta FE_{app}}{RT}\right)}} \qquad [25]$$

Nevertheless, the "S" shape behavior, resulting in the observed current maximum, is only present in a narrow pH range and disappears both at more acidic and also in more alkaline environments.[23,47,52] In the acidic solutions purged with N_2, the reports in the literature[26,49,58] suggest a 0.5 order dependence on H^+ concentration, which is in accordance with that seen in the experimental results in the present study. On the other hand, in the CO_2-saturated solutions the current maxima do not exhibit any significant pH dependence (Figure 3 and Figure 6),
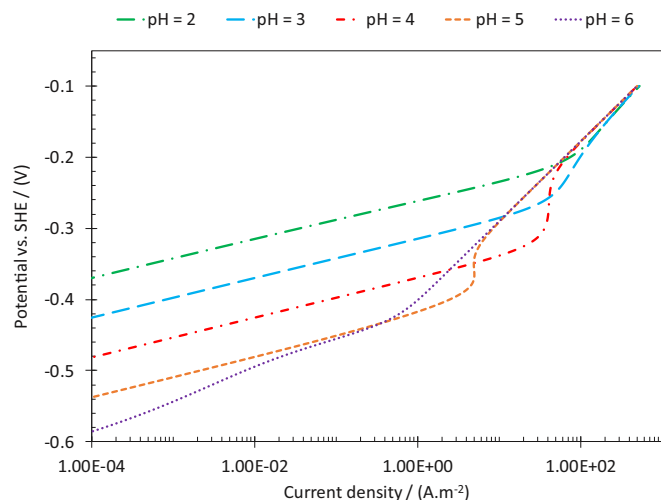
Figure 9. The calculated anodic polarization curve in a N_2-saturated acidic solutions at 10°C.

Figure 10. The calculated anodic polarization curve, in CO_2-saturated acidic solutions at 10°C, at pH 4 and 5, $pCO_2 = 1$ bar (long dashed lines), $pCO_2 = 5$ bar (dotted-dashed lines), and $pCO_2 = 15$ bar (dashed lines).

yet the previously reported results showed that this current maximum no longer exists at higher pH values.[23] Based on such observations, one can conclude that the active dissolution range and the current maximum are also affected by a secondary process with a rate that rapidly decreases with increasing pH. This can be due to the change in the rate determining step, as noted previously,[47,50,52] where the increased pH reduces the rate of reaction in the active dissolution range. Hence, its corresponding rate can also be expressed by the same generic form of Equation 24. The observed net rate resulting from these two processes can be calculated based on the harmonic average of both reaction rates in order to reflect the consecutive nature of these reactions. The net anodic current can therefore be expressed as Equation 26.

$$i_a = \left(\frac{1}{(1-\theta)\,i_1} + \frac{1}{(1-\theta)\,i_2} \right)^{-1} + \theta i_3 \qquad [26]$$

Figure 9 demonstrates the results of a mathematical simulation of anodic polarization curves based on the rate expression presented above for a N_2 saturated acidic solution, while the performance of the complete model is discussed in the following sections. By finding the best fit to the experimental data, the anodic current density in the active dissolution range obtained using the harmonic average of an electrochemical process, is expressed as Equation 24, with $m_{H^+,1} = -2$ and $\alpha_1 = 2$, and another with $m_{H^+,2} = 1$ and $\alpha_2 = 1$. The Langmuir isotherm in the form of Equation 25 is represented with $m_{H^+,\theta} = -2$ and $\alpha_\theta = 2$. And finally, the current densities in the pre-passivation range were obtained using $m_{H^+,3} = 0$ and $\alpha_3 = 0.5$.

As shown in Figure 9, the semi-empirical calculation of the anodic current density is able to reflect the observed potential and pH dependence at both the lower and higher current densities with a reasonably predicted transition state in-between. Nevertheless, some deviations from experimental data, especially in the transition state would be expected due to the simplified mechanistic view behind these calculations, which disregards specific reaction steps and ignores intermediate species of lesser significance.

The case of iron dissolution in CO_2-saturated solution is even more complex than that in N_2-saturated solution, with many important aspects yet to be understood. However, considering that the general behavior of anodic polarization curves are similar in both N_2 and CO_2 saturated solutions, the anodic current density for the latter case may also be calculated based on Equation 26. The observed differences, including the dependence on CO_2 concentration were accounted for in the rate expressions. Nevertheless, the carbonate species (CO_2, H_2CO_3, HCO_3^-, and CO_3^{2-}) responsible for such an effect cannot be explicitly identified. For the lack of a better understanding, the rate expressions were represented in terms of the dissolved CO_2 concentra-
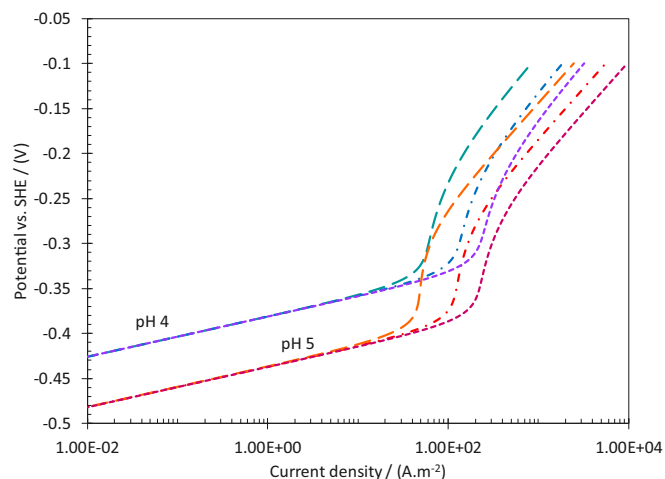
tion (Equation 27). The expressions for electrochemical reactions and the Langmuir isotherm were reworked for the case of CO_2-saturated solutions as:

$$i_{a,j} = n_{Fe} F k_j C_{H^+}^{s\ m_{H^+,j}} C_{CO_2}^{s\ m_{CO_2,j}} e^{\left(\frac{\alpha_j F E_{app}}{RT} \right)} \qquad [27]$$

$$\theta = \frac{K_\theta C_{H^+}^{s\ m_{H^+,\theta}} C_{CO_2}^{s\ m_{CO_2,\theta}} e^{\left(\frac{\alpha_\theta F E_{app}}{RT} \right)}}{1 + K_\theta C_{H^+}^{s\ m_{H^+,\theta}} C_{CO_2}^{s\ m_{CO_2,\theta}} e^{\left(\frac{\alpha_\theta F E_{app}}{RT} \right)}} \qquad [28]$$

Figure 10 shows the results of a mathematical simulation of anodic polarization curves in CO_2-saturated solutions. The current density in the active dissolution range is obtained using the harmonic average of an electrochemical process with $m_{H^+,1} = -2.5$, $m_{CO_2,1} = 0$ and $\alpha_1 = 2.5$, and another with $m_{H^+,2} = 1$, $m_{CO_2,2} = 0.5$ and $\alpha_2 = 2$. The Langmuir isotherm in the form of Equation 28 is represented with $m_{H^+,\theta} = -2.5$, $m_{CO_2,\theta} = -0.5$ and $\alpha_\theta = 2.5$, and finally, the current densities in the pre-passivation range is obtained using $m_{H^+,3} = -0.5$, $m_{CO_2,3} = 0.5$ and $\alpha_3 = 0.5$. Figure 10 demonstrates the performance of the present approach with the change in pH and partial pressure of CO_2, as it relates to the conditions of the present study.

The results obtained in this fashion were able to reasonably represent the general behavior observed at the conditions of the present study. The elements used in the present model can be modified to incorporate new mechanistic understanding of this reaction as it becomes available, in order to improve the range of validity of the results.

The model used in this study is built based on only two key electrochemical reaction: the H^+ reduction and Fe oxidation. The rates of these reactions in aqueous acidic solutions can be obtained as discussed above. Considering the heterogeneity of the corrosion process and the underlying electrochemical reactions, these expressions are included in the model as the metal surface boundary conditions, where the flux of the species (N_i as discussed in detail in section Mass transfer and the buffering effect in the boundary layer) at the electrode are defined by the rate of these electrochemical reactions. That can be mathematically expressed as:

$$N_i |_{x=0} = -\frac{s_{ij} i_j}{n_j F} \qquad [29]$$

Equation 29 relates the current density of reaction j (H^+ reduction or Fe oxidation) to the flux of the involved electroactive species at the metal surface, where s_{ij} is the stoichiometric coefficient of species i, and n_j is the number of transferred electrons. The negative sign is to compensate for the sign convention, where anodic currents are represented with

Table IV. The equilibrium parameters for H₂O/CO₂ system.⁺

Param.	$H^*_{CO_2^*}$ [71] [m.bar^{-1}]	ϕ_{CO_2} [31] -	K_{hyd} [37] -	K^*_{ca} [72] [m]	K_{bi} [72] [m]	K_w [73] [m²]	P_{ws} [74,75] [bar]
a_1 ⁺⁺	1.3000 E1	1.0000	1.02E4	233.51593	−151.1815	−4.098	1.167 E3
a_2	−1.3341 E-2	4.7587 E-3	−55.7	0.0000	−0.0887	−3245.2	−7.242 E5
a_3	−5.5898 E2	−3.3570 E-6	NA	−11974.3835	−1362.2591	2.2362	−1.707 E1
a_4	−4.2258 E5	0.0000	NA	0.0000	0.0000	−3.984 E7	1.202 E5
a_5	NA	−1.3179	NA	−36.5063	27.7980	13.957	−3.233 E6
a_6	NA	−3.8389 E-6	NA	−450.8005	−29.5145	8.5641 E5	1.492 E1
a_7	NA	0.0000	NA	21313.1885	1389.0154	NA	−4.823 E3
a_8	NA	2.2815 E-3	NA	67.1427	4.4196	NA	4.051 E5
a_9	NA	0.0000	NA	0.0084	0.0032	NA	−2.386 E-1
a_{10}	NA	0.0000	NA	−0.4015	−0.1644	NA	6.502 E2
a_{11}	NA	0.0000	NA	−0.0012	−0.0005	NA	NA

⁺The equilibrium constants are based on molal concentrations. Appropriate unit conversion should be considered whenever necessary.
⁺⁺The a_i values are rounded to four digits after the decimal.
†$\ln(K^*_{H,CO_2^*}) = a_1 + a_2 T + \frac{a_3}{T} + \frac{a_4}{T^2}$.
††$\phi_{CO_2} = a_1 + [a_2 + a_3 T + \frac{a_4}{T} + \frac{a_5}{T-150}]P + [a_6 + a_7 T + \frac{a_8}{T}]P^2$.
†††$K_{hyd} = 55.6\, exp(\frac{-a_1 + a_2\,T}{RT})$.
♮$\ln(par.) = a_1 + a_2\,T + \frac{a_3}{T} + \frac{a_4}{T^2} + a_5 \ln(T) + (\frac{a_6}{T} + \frac{a_7}{T^2} + \frac{a_8}{T} lnT\,) + (\frac{a_9}{T} + \frac{a_{10}}{T^2} + \frac{a_{11}}{T} lnT\,)(p - p_s)^2$.
$P_s = 1$ if $T<373.15$, $P_s = P_{ws}$ if $T>373.15$.
♮♮$-\log(K_w) = a_1 + \frac{a_2}{T} + \frac{a_3}{T^2} + \frac{a_4}{T^3} + (a_5 + \frac{a_6}{T} + \frac{a_7}{T^2})\log(10^{-3}\rho_w)$.
♭$P_{ws} = 10\,[\frac{2C}{-B+(B^2-4AC)^{0.5}}]^4$.
$A = \theta^2 + a_1\theta + a_2; B = a_3\theta^2 + a_4\theta + a_5; C = a_6\theta^2 + a_7\theta + a_8; \theta = T + \frac{a_9}{T-a_{10}}$.

positive values and cathodic currents with negative values. For the chemical species that are not involved in electrochemical reactions the flux at the metal surface is zero:

$$N_i|_{x=0} = 0 \qquad [30]$$

The kinetic parameters for the H⁺ reduction reaction expressed in the form of Equation 23 were obtained by finding the best fit of the model to the experimental data, with the temperature effect expressed in terms of the van't Hoff equation (Equation 31). The values of $k_{H^+} = 2E-8\ mol/m^2\ s\ (\frac{mol}{m^3})^{1-m_{H^+}}$, $m_{H^+} = 0.5$, $\alpha_{H^+} = 0.43$, and the reaction enthalpy of $\Delta H = 100.3\,kJ$ with $T_{ref} = 283^oK$ was obtained, which were found to be in reasonable agreement with those obtained in glass cell experiments presented in an earlier study.[17]

$$k_j|_T = k_j|_{T_{ref}}\, e^{\frac{-\Delta H_j}{R(T-T_{ref})}} \qquad [31]$$

In a similar fashion, the kinetic parameters for the iron dissolution reaction were obtained as listed in Table V. The rate of this reaction, and its pH and pCO₂ dependence were expressed as discussed above. The four kinetic and equilibrium constants were obtained with a reasonable confidence based on a corresponding characteristic feature in the polarization curves. Considering the significantly different apparent Tafel slopes and pH dependence observed in N₂-saturated and CO₂-saturated solutions, two sets of kinetic parameters were used to represent the rate of this reaction.

Mass transfer and the buffering effect in the boundary layer.— In order to calculate the rate of electrochemical reactions, the surface concentrations of the electroactive species are required. They can be calculated by using mass conservation laws inside the diffusion boundary layer that is stretching from the metal surface to the bulk solution, given the known solution speciation in the bulk (as discussed in the solution speciation section). The mass conservation law inside the diffusion boundary layer of an electrochemical system is described via the Nernst-Planck Equation as:

$$\frac{\partial C_i}{\partial t} = -\nabla.N_i + R_i \qquad [32]$$

where N_i is the flux of species i, and R_i is the rate of its production/consumption via chemical reactions that incorporates the effect of CO₂ hydration reaction and the carbonic acid buffering effect. The flux is typically expressed as:[59]

$$N_i = -z_i u_i F C_i \nabla\phi - D_i \nabla C_i + v C_i \qquad [33]$$

The first term in Equation 33 is the contribution of electro-migration for the ionic species i with charge of z_i and mobility of u_i, in the presence of an electric field ($\nabla\phi$), where F is the Faraday's constant. The second term is the molecular diffusion arising from the concentration gradient, with D_i being the diffusion coefficient. The last term represents the effect of convective flow with the velocity of v.

In a fully developed turbulent flow regime such as the one inside a pipe or the thin channel cell used in the present study, specifying the velocity profile inside the boundary layer requires extensive fluid mechanics calculations. In the alternative approach used in this study, the effect of flow is represented by the concept of eddy diffusivity. Unlike laminar flow that moves the bulk of the fluid toward a certain direction, the eddies in turbulent flow mix the solution at a microscale. The effect of turbulent transport is therefore expressed by an analogy to molecular diffusion, with D_e representing the eddy diffusivity. Hence, Equation 33 in turbulent flow is restated as:

$$N_i = -z_i u_i F C_i \nabla\phi - (D_i + D_e)\nabla C_i \qquad [34]$$

Considering one dimensional nature of a fully developed diffusion boundary layer, only the direction normal to the metal surface is significant in Equations 32 and 34. Assuming an ideal solution, the ionic mobility can be expressed via Nernst-Einstein relationship ($u_i = D_i/RT$). Equations 32 and 34 can be simplified for the case of a one dimensional semi-infinite domain normal to the electrode surface as:

$$N_i = -(D_i + D_e)\frac{\partial C_i}{\partial x} - \frac{z_i D_i F C_i}{RT}\frac{\partial\phi}{\partial x} \qquad [35]$$

$$\frac{\partial C_i}{\partial t} = \frac{\partial}{\partial x}\left((D_i + D_e)\frac{\partial C_i}{\partial x}\right) + \frac{z_i D_i F}{RT}\frac{\partial}{\partial x}\left(C_i\frac{\partial\phi}{\partial x}\right) + R_i \qquad [36]$$

The diffusion coefficients appearing in Equations 35 and 36 for the species of significance in the present study are listed in Table VI. The

Table V. Kinetic parameters of the iron dissolution reaction in acidic solutions.

	N$_2$-saturated environment		CO$_2$-saturated environment	
	$k_{0,ref}$	ΔH (kJ) at $T_{ref} = 283$	$k_{0,ref}$	ΔH (kJ) at $T_{ref} = 283$
k_1	1.5E6	42.9	3.0E9	42.9
k_2	4.0E5	12.1	1E13	6.1
k_3	5E-2	39.2	4.5E-3	30.2
K_θ	1.5E10	10.2	4.0E13	24.7

temperature dependence of molecular diffusivity (D_i) can be expressed on the basis of the well-known Stokes-Einstein relationship as:

$$\frac{D_{i,T}}{D_{i,298}} = \frac{T}{298} \frac{\mu_{298}}{\mu_T} \qquad [37]$$

where T is the temperature in degree Kelvin, and μ_T is the water viscosity at T.

The eddy diffusivity distribution throughout the boundary layer of a fully developed turbulent flow can be obtained from the empirical equation suggested by Arvanith:[60]

$$D_e = \nu \frac{0.0007 \, x^{+3}}{\left[1 + 0.00405x^{+2}\right]^{1/2}} \qquad [38]$$

where ν is the kinematic viscosity, and x^+ is the dimensionless distance from the wall defined as:

$$x^+ = \frac{x \left(\tau_w / \rho\right)^{1/2}}{\nu} \qquad [39]$$

Equation 38 is valid for $x^+ < 30$ and it is universal in turbulent flow when appropriate dimensionless parameters are used. The influence of the geometry of channel flow appears in the wall shear stress term (τ_w) of Equation 39. Where τ_w is defined as a function of Fanning friction factor (C_f) as shown in Equation 40, and the Fanning friction factor itself is a function of the Reynolds number (Re). The Reynolds number carries the geometry specific information in this set of equations.
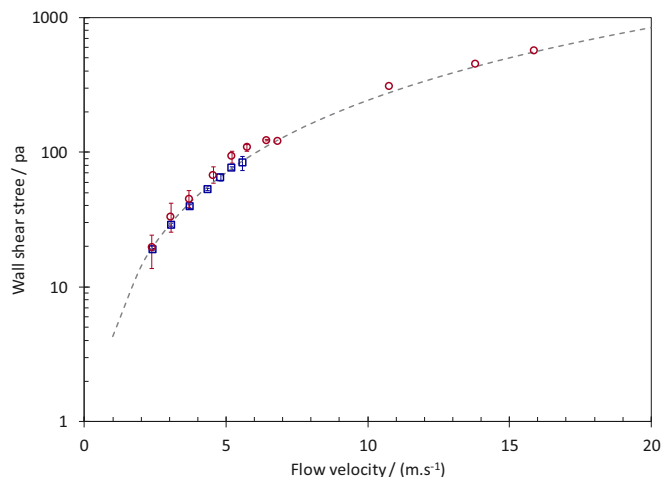
$$\tau_w = \frac{1}{2}\rho C_f V^2 \qquad [40]$$

In Equation 40, V is the average flow velocity (m.s^{-1}), and ρ is the fluid density (kg/m^3). There are a few different empirical relationships proposed for calculating the friction factor in a turbulent flow regime. In the present study, the correlation of Swamee and Jain[61] for Darcy friction factor ($C_d = 4C_f$) was used (Equation 41), which is essentially an explicit derivation of the well-known Colebrook-White correlation.[62] The Reynolds number (Re = $V.D_{eq}/\nu$) was calculated based on the equivalent characteristic diameter: $D_{eq} = 4A/P$, where A and P are the cross section area and the interior perimeter of the thin channel. The first term in the logarithm in Equation 41 accounts for the effect of wall roughness (ε) on the friction factor.

$$C_d = 0.25 \left[\log \left(\frac{\varepsilon/D_{eq}}{3.7} + \frac{5.74}{Re^{0.9}} \right) \right]^{-2} \qquad [41]$$

For the purposes of validation, the wall shear stress calculated using Equations 40 and 41 is compared with the experimental data for the thin channel flow cell used in the present study, in Figure 11. The experimental data shown in Figure 11 were recalculated from the data obtained in earlier studies in the same thin channel flow cell.[63–66] The experimental data were obtained via pressure drop measurements and also by using a floating element wall shear stress probe (Lenterra Inc.), as described in detail in the original studies.[63–66]

The R_i term in Equation 36 represents the effect of the homogeneous chemical reactions as a source/sink of the chemical species. The rate of each chemical reaction j in the general form of Reaction 42 can

Figure 11. The comparison of the calculated and measured wall shear stress in the thin channel flow cell used in the present study. Experimental data from Li[63] and Akeer.[65]

be calculated as shown in Equation 43.

$$\sum_{r=1}^{n_r} C_r \rightleftharpoons \sum_{p=1}^{n_p} C_p \qquad [42]$$

$$R_j = k_{f,j} \prod_{r=1}^{n_r} C_r - k_{b,j} \prod_{p=1}^{n_p} C_p \qquad [43]$$

The rate of production (or consumption) of every species i (R_i) for j chemical reactions shown as Reactions 4 to 7, may be expressed in a matrix format as Equation 44. The kinetic rate constants for these chemical reactions can be found in Table VII.

$$\begin{bmatrix} R_{CO_{2(aq)}} \\ R_{H^+_{(aq)}} \\ R_{H_2CO_{3(aq)}} \\ R_{HCO^-_{3(aq)}} \\ R_{CO^{2-}_{3(aq)}} \\ R_{OH^-_{(aq)}} \end{bmatrix} = \begin{bmatrix} -1 & 0 & 0 & 0 \\ 0 & 1 & 1 & 1 \\ 1 & -1 & 0 & 0 \\ 0 & 1 & -1 & 0 \\ 0 & 0 & 1 & 0 \\ 0 & 0 & 0 & 1 \end{bmatrix} \times \begin{bmatrix} R_{hyd} \\ R_{ca} \\ R_{bi} \\ R_w \end{bmatrix} \qquad [44]$$

Considering the discussion above, Equation 36 can be used to describe the concentration distribution of all the involved chemical species inside the boundary layer (one such equation needs to be considered for every species in solution). The potential inside the boundary layer can be specified with the aid of the electro-neutrality Equation 17. The electro-neutrality equation applied in the diffusion boundary layer is in fact derived from the more theoretically valid Poisson's equation, assuming that the typical potential gradient in a finite element of the solution is not large enough to result in any significant change in the charge density (charge density = 0 as shown in Equation 17).[4] In

Table VI. Reference diffusion coefficients at 25°C.

Species	Diffusion coefficient in water $\times 10^9$ (m^2/s)	Reference
CO_2	1.92	76
H_2CO_3	1.75	Estimated
HCO_3^-	1.185	77
CO_3^{2-}	0.923	77
H^+	9.312	59
OH^-	5.273	77
Na^+	1.334	59
Cl^-	2.032	59,77
Fe^{2+}	0.72	59

Table VII. Kinetic rate constants of Reactions 4 to 7. k_f denotes the reaction progress from left to right and $K = k_f/k_b$.

Reaction #	Reaction rate constant	reference
4	$k_{f,hyd} = 1.28E11 \; e^{\left(\frac{81200}{RT}\right)} \; (1/s)$	37
5	$k_{b,ca} = 4.7 \times 10^{10} \quad (1/M.s)$	78–80
6	$k_{b,bi} = 5.0 \times 10^{10} \quad (1/M.s)$	78,80
7	$k_{b,w} = 1.4 \times 10^{11} \quad (1/M.s)$	79,81

the typical conditions of CO_2 corrosion, especially when significant amounts of ionic species are present, this assumption is generally valid.

Mathematical methods.—The mathematical equations as described in the previous section form a set of non-linear, coupled, partial differential equations. The following set of dimensionless variables were defined to replace distance (x), concentration (C_i), and potential (E and ϕ).

$$X = \frac{x}{\delta} \quad \xi_i = \frac{C_i}{C_i^b} \quad \Phi = \frac{F\phi}{RT} \quad \psi = \frac{FE_{app}}{RT}$$

The resulting set of differential equations must be solved numerically. With the simple one-dimensional geometry spanning from the metal surface toward the bulk solution, the finite difference method can be used to solve the equations. This method is commonplace in mathematical modeling of electrochemical systems,[67–69] and has been discussed in detail elsewhere.[59,70]

Considering the heterogeneous nature of the metallic CO_2 corrosion and the fast kinetics of the involved homogenous chemical reactions, the concentration gradient in the solution in the vicinity of the metal surface can be large. In order to capture the effect of homogeneous chemical reactions, it is necessary to have sufficient number of nodes inside the reaction boundary layer. That can be achieved simply by increasing the number of spatial nodes. The alternative approach, used in the present study, is to employ a non-uniform grid with a finer grid close to the metal surface and coarser increments as the bulk solution is approached. The latter method can significantly improve the stability and the computational time of the model. The partial differential equations are discretized using second order, non-uniform, Taylor's series approximations, resulting into a set of algebraic equations. In the present model the grid size was allowed to grow linearly with a factor of 1.1 from the initial value of X = 1.0E-4. The non-uniform grid derivative approximations used in the present study are shown in Table VIII for a function $f(x)$, where $\Delta x_j = x_j - x_{j-1}$ is the distance between the two adjacent nodes.

The discretized equations can further be transformed into a matrix format. The final solution can then be obtained through various solution algorithms such as Neman's "Band-J" open source code where the coefficient matrix is developed and inverted by LU decomposition method.[59,70]

The temporal derivation was expressed using Euler's approximation, in the present study. Considering that the equations are non-linear, the solution at each time step was obtained iteratively, using an explicit approach.

Model verification .—The model predictions are compared with the experimental data, as shown in Figure 12 to Figure 14. Figure 12
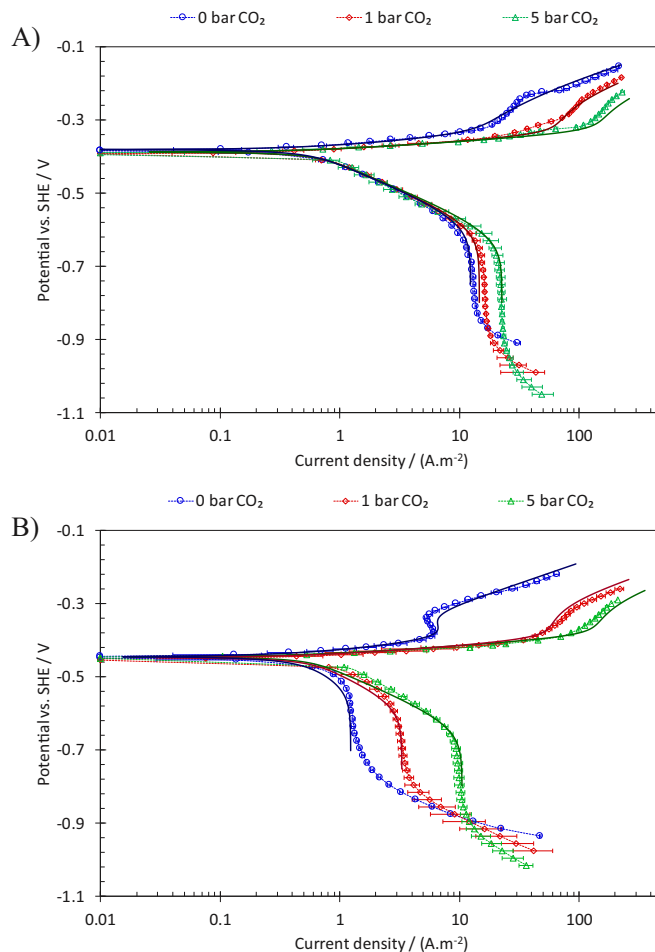
Figure 12. The comparison of the simulated polarization curves (solid lines) with the experimental data obtained on API 5L X65 mild steel in acidic solutions, at 10°C, 12.9 m.s^{-1} flow velocity, 0.1 M NaCl, and varying pCO$_2$. A) at pH 4. B) at pH 5. Error bars represent the standard deviation of three repeated experiments at selected potentials.

demonstrates the results obtained at 10°C, which are of particular interest in the present study. At this condition the charge transfer controlled current densities were clearly observed, which were found to be independent of the partial pressure of CO_2. It was based on this observation that the direct reduction of H_2CO_3 was considered to be insignificant. Accordingly, the quantitative analysis of the results showed that both the charge transfer controlled cathodic currents and the limiting current densities can be adequately estimated considering only the H^+ reduction, when the homogeneous chemical reactions are properly incorporated in the model. The estimated anodic current densities were also in good agreement with the experimental data, with the effect of CO_2 being predicted by the model reasonably well.

The effect of temperature on the polarization curves at 5 bar CO_2 is shown in Figure 13, where the results from 10°C and 30°C measurements were compared at pH 4 and pH 5. The effect of temperature

Table VIII. Derivative approximation for a non-uniform grid.

First order derivative, central approximation

$a_i = -\frac{\Delta x_{i+1}}{\Delta x_i(\Delta x_i + \Delta x_{i+1})}$

First order derivative, three point forward approximation

$a_i = -\frac{2\Delta x_{i+1} + \Delta x_{i+2}}{\Delta x_{i+1}(\Delta x_{i+1} + \Delta x_{i+2})}$

Second order derivative, central approximation

$a_i = \frac{2}{\Delta x_i(\Delta x_i + \Delta x_{i+1})}$

$f'(x_i) = a_i f(x_{i-1}) + b_i f(x_i) + c_i f(x_{i+1})$
$b_i = \frac{\Delta x_{i+1} - \Delta x_i}{\Delta x_i \Delta x_{i+1}}$ $\qquad c_i = \frac{\Delta x_i}{\Delta x_{i+1}(\Delta x_i + \Delta x_{i+1})}$

$f'(x_i) = a_i f(x_i) + b_i f(x_{i+1}) + c_i f(x_{i+2})$
$b_i = \frac{\Delta x_{i+1} + \Delta x_{i+2}}{\Delta x_{i+1} \Delta x_{i+2}}$ $\qquad c_i = -\frac{\Delta x_{i+1}}{\Delta x_{i+2}(\Delta x_{i+1} + \Delta x_{i+2})}$

$f''(x_i) = a_i f(x_{i-1}) + b_i f(x_i) + c_i f(x_{i+1})$
$b_i = -\frac{2}{\Delta x_i \Delta x_{i+1}}$ $\qquad c_i = \frac{2}{\Delta x_{i+1}(\Delta x_i + \Delta x_{i+1})}$
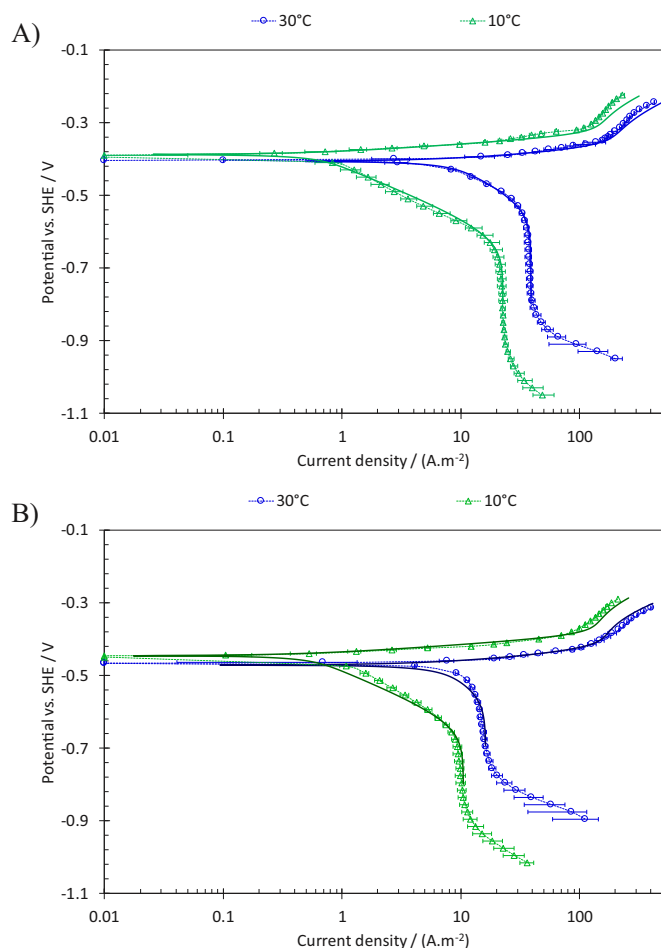
Figure 13. The comparison of the simulated polarization curves (solid lines) with the experimental data obtained on API 5L X65 mild steel in acidic solutions, 12.9 m.s^{-1} flow velocity, 0.1 M NaCl, 5 bar pCO$_2$. A) at pH 4. B) at pH 5. Error bars represent the standard deviation of three repeated experiments at selected potentials.

Figure 14. The comparison of the experimental and estimated corrosion rates on API 5L X65 mils steel, in 0.1 M NaCl solutions and 12.9 m.s^{-1} flow velocity. A) at pH 4, and B) at pH 5. The solid bars show the experimental data and the dashed bars show the predicted values. Error bars represent the standard deviation of at least five repeated measurements.

on the cathodic limiting current density is through the physical properties of the water and also via the chemical equilibrium associated with H$_2$O/CO$_2$ system, which was estimated successfully at both conditions. The changes in electrochemical reaction rates are calculated through van't Hoff equation as discussed earlier in the text.

Ultimately, the model developed above was used to calculate the corrosion rates as shown in Figure 14 to Figure 16. Figure 14 is the comparison of the calculated corrosion rates with those obtained experimentally at the conditions of the present study. The model was found to be successfully predicting the corrosion rates with reasonable accuracy. Also, the transition from the charge transfer controlled corrosion scenario, which is the predominant corrosion mechanism in low temperatures, to the mass transfer controlled corrosion mechanism, observed at higher temperatures, was properly reflected in the corrosion rate calculations. The significance of this behavior is further demonstrated in Figure 15, where the predicted corrosion rates at pH 5 as a function of pCO$_2$ are shown at various temperatures.

As is apparent in Figure 15, the corrosion at low temperatures is under charge transfer control nearly over the whole pCO$_2$ range; hence, it does not show any significant dependence on pCO$_2$. As the temperature is increased, the corrosion rates at lower pCO$_2$ values become mass transfer limited, which is indicated by the rapidly increasing rates with increasing pCO$_2$, as a result of buffering effect of CO$_2$ and H$_2$CO$_3$. The pCO$_2$ threshold where the corrosion rate gets into the charge transfer controlled range is strongly dependent on the environmental conditions such as temperature, as shown in Figure 15,
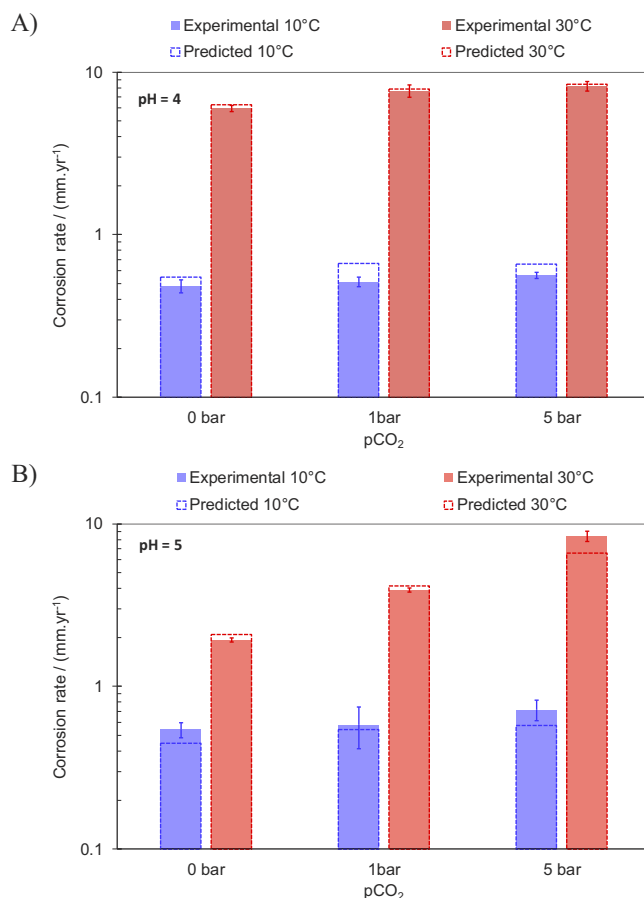
or other parameters such as flow velocity and the presence of organic acids. In the conditions considered here, the charge transfer controlled rate for the corrosion process (maximum corrosion rate) is reached at approximately 5 bar CO$_2$ at 30°C, while at 60°C the transition is not clearly observed even at pCO$_2$ as high as 10 bar.
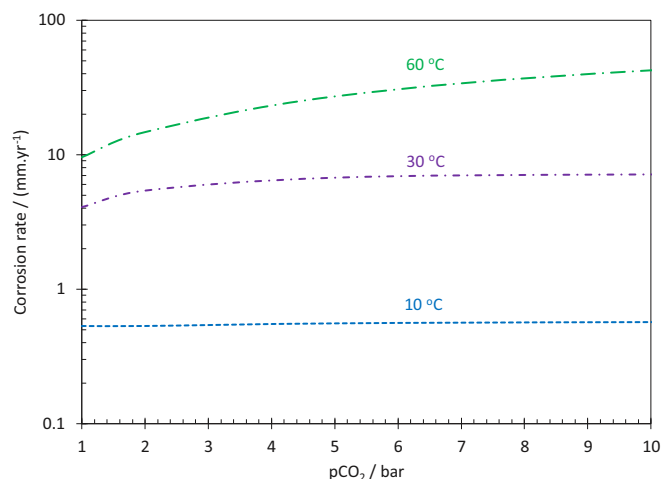

Figure 15. The effect of temperature on the predicted corrosion rates at pH 5, 0.1 M NaCl and 12.9 m.s^{-1} flow velocity.
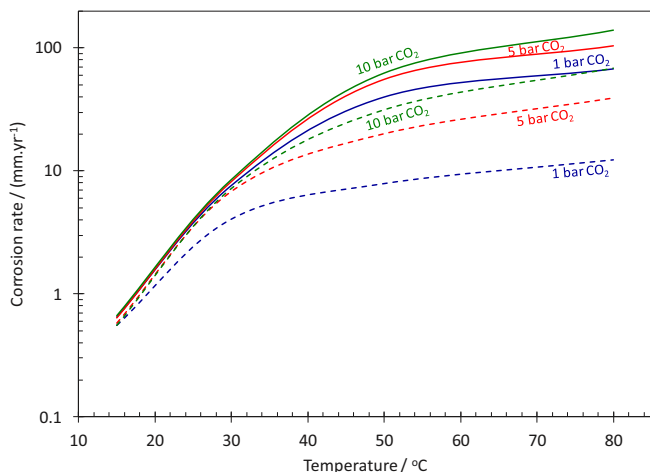
Figure 16. The effect of temperature on the predicted corrosion rates at pH 4 (solid lines) and pH 5 (dashed lines), at 0.1 M NaCl and 12.9 m.s^{-1} flow velocity.

The effect of pH on the transition from charge transfer controlled corrosion rate, where the presence of H$_2$CO$_3$ has negligible effect on the observed corrosion rates, to mass transfer controlled corrosion rate, where the buffering effect of carbonic acid has a determinant effect on corrosion rates, is shown in Figure 16. The results demonstrate that, while at lower pH the corrosion rates are generally higher, they are less affected by the pCO$_2$. Moreover, the transition temperature to the mass transfer controlled scenario is higher. This behavior is expected since the H$^+$ reduction rate is higher at higher concentration of this species, and the limiting current is defined predominantly by the mass transfer of H$^+$. A significant effect of H$_2$CO$_3$ on the corrosion rate is only observed at higher temperature and pCO$_2$. This behavior leads to more practically important conclusions: even though the direct reduction of carbonic acid is shown to be insignificant, the pCO$_2$ would remain one of the main parameters in corrosion rate prediction in the common industrial conditions due to its significant buffering ability and also its influence on the behavior of the iron dissolution reaction. Elevated temperatures and near neutral pH values are very common conditions in oil and gas production and transmission facilities. At such conditions, the cathodic current is significantly influenced by mass transfer, and the anodic current is most likely in the transition/pre-passivation range, both of which are significantly affected by the presence of CO$_2$. Hence, although H$_2$CO$_3$ is not directly reduced, corrosion rates are still significantly influenced by pCO$_2$ in most practical conditions. The latter also signifies the importance of the proper accounting of the chemical reactions inside the diffusion layer when calculating the corrosion rates. That can be achieved by using comprehensive mathematical models, similar to the one developed in the present study. The earlier more simple mechanistic modeling approaches[7,16,22] do not allow for proper description of the buffering effect, as discussed in more detail elsewhere.[3,4]

Conclusions

• The electrochemical activity of H$_2$CO$_3$ reduction on a mild steel surface was investigated based on the behavior of charge transfer controlled range of the cathodic polarization curves in CO$_2$-saturated solutions.

• The experimental results did not show any indications to suggest H$_2$CO$_3$ is reduced during cathodic polarization, in accordance with the so-called "buffering effect" mechanism.

• The effect of CO$_2$ on the anodic polarization curves, especially that observed in the transition and pre-passivation ranges was confirmed in the experimental results of the present study.

• These mechanistic observations were used in development of a comprehensive mathematical model in order to provide further quantitative support. The simulated polarization curves and the estimated corrosion rates were found to agree well with those obtained experimentally.

• The significance of these mechanistic observations was further discussed based on the estimated corrosion rates of the model. The pCO$_2$ dependence of corrosion rates was shown to be strongly temperature dependent. At low temperatures and pH values below 5, corrosion rates may not be significantly influenced by pCO$_2$, which is due to the anodic current being in the active dissolution range and the cathodic current being under charge transfer control. On the other hand, at elevated temperature a significant pCO$_2$ dependence of the corrosion rate could be expected. That is the result of the shift of corrosion current to the transition/pre-passivation range of the iron dissolution reaction and at the same time, the shift of the corrosion current into the mass transfer controlled cathodic current, both of which are significantly increased in the presence of CO$_2$.

List of Symbols

A (m^2)	Electrode Surface area
B	Stern-Geary coefficient
b_j	Tafel slope of reaction j
CR $(mm.yr^{-1})$	Corrosion rate
C_d	Darcy friction factor
C_f	Friction factor
c_i $(mol.m^3)$ *(unless stated otherwise)*	Concentration of species i
c_i^s $(mol.m^3)$ *(unless stated otherwise)*	Surface concentration of species i
c_i^b $(mol.m^3)$ *(unless stated otherwise)*	Bulk concentration of species i
D_i $(m^2.s^{-1})$	Diffusion coefficient of species i
D_e $(m^2.s^{-1})$	Eddy diffusivity
D_{eq} (m)	Equivalent hydrodynamic length
E_{app} (V)	Applied potential
F	Faraday's constant
H_{CO_2} $(m.bar^{-1})$	CO2 Henry's Constant
ΔH_j (kJ)	Enthalpy of reaction j
i_j $(A.m^2)$	Current density of reaction j
m_i	Reaction order with respect to species i
K_j	Equilibrium constants of reaction j
k_j $(varies)$	Kinetic rate constant of reaction j
N_i $(mol.m^{-2})$	Flux of species i
n_j	Number of transferred electrons in reaction j
n_r	Number of reactants
n_p	Number of products
P_n	Product n
P_{ws} (bar)	Water saturation pressure
p_i (bar)	Partial pressure of species i

R $(j.K^{-1}.mol^{-1})$	Universal gas constant
R_p (Ω)	Polarization resistance
R_m	Reactant m
R_i $(mol.m^{-3})$	Rate of production/consumption of species i through chemical reactions
R_j $(mol.m^{-3})$	Rate of reaction j
Re	Reynolds number
s_{ij}	Stoichiometric coefficient of species i in reaction j
T (K)	Absolut temperature
T_{ref} (K)	Absolute reference temperature
t (s)	Time
v $(m.s^{-1})$	Velocity vector
V $(m.s^{-1})$	Average flow velocity
X	Dimensionless normalized distance
x (m)	Spatial domain
x^+	Dimensionless distance from the wall
u_i $(m.s^{-1})$	Mobility of species i
z_i	Ionic charge of species i

Greek

α_a (V)	Charge transfer coefficient
δ (m)	Boundary layer thickness
ε	Surface roughness
θ	Fractional surface coverage
μ_T (cp)	Water viscosity at temperature T
ν $(m^2.s^{-1})$	Kinematic viscosity
ξ_i	Dimensionless normalized concentration
ρ $(kg.m^3)$	Water density
$\tau_w (Pa)$	Wall shear stress
Φ	Dimensionless potential inside the electrolyte
φ_i	Fugacity coefficient of species i
ϕ (V)	Potential inside the electrolyte
ψ	Dimensionless applied potential

ORCID

Aria Kahyarian   https://orcid.org/0000-0001-8809-1493

References

1. C. de Waard and D. E. Milliams, in *Internal and External Protection of Pipes*, p. F1-1-F1-8 (1975).
2. C. de Waard and D. E. Milliams, *Corrosion*, **31**, 177 (1975).
3. A. Kahyarian, M. Singer, and S. Nesic, *J. Nat. Gas Sci. Eng.*, **29**, 530 (2016).
4. A. Kahyarian, M. Achour, and S. Nesic, in *Trends in Oil and Gas Corrosion Research and Technologies*, A. M. El-Sherik, p. 805, Elsevier (2017).
5. A. Kahyarian, M. Achour, and S. Nesic, in *Trends in Oil and Gas Corrosion Research and Technologies*, A. M. El-Sherik, p. 149, Elsevier (2017).
6. G. Schmitt and B. Rothmann, *Werkstoffe und korrosion*, **28**, 816 (1977).
7. L. G. S. Gray, B. G. Anderson, M. J. Danysh, and P. R. Tremaine, in *Corrosion*, Paper No. 464 (1989).
8. M. Nordsveen, S. Nešić, R. Nyborg, and A. Stangeland, *Corrosion*, **59**, 443 (2003).
9. S. Nešić, M. Nordsveen, R. Nyborg, and A. Stangeland, in *Corrosion*, Paper No. 040 (2001).
10. B. F. M. Pots, in *Corrosion*, Paper No. 137 (1995).
11. S. Turgoose, R. A. Cottis, and K. Lawson, in *Computer modeling in corrosion, ASTM STP 1154*, p. 67 (1992).
12. E. Remita, B. Tribollet, E. Sutter, F. Ropital, X. Longaygue, J. Kittel, C. Taravel-Condat, and N. Desamais, *Corros. Sci.*, **50**, 1433 (2008).
13. T. Tran, B. Brown, and S. Nešić, in *Corrosion*, Paper No. 671 (2015).
14. A. Kahyarian, B. Brown, S. Nesic, and S. Nesic, *Corrosion*, **74**, 851 (2018).
15. A. Kahyarian, B. Brown, and S. Nesic, *Corrosion*, Paper No. 11232 (2018).
16. L. G. S. Gray, B. G. Anderson, M. J. Danysh, and P. R. Tremaine, in *Corrosion*, Paper No. 40 (1990).
17. A. Kahyarian, A. Schumaker, B. Brown, and S. Nesic, *Electrochim. Acta*, **258**, 639 (2017).
18. A. Kahyarian, B. Brown, and S. Nesic, *Corrosion*, **72**, 1539 (2016).
19. T. Tran, B. Brown, S. Nešić, and B. Tribollet, *Corrosion*, **70**, 223 (2014).
20. A. Kahyarian, B. Brown, and S. Nesic, *J. Electrochem. Soc.*, **164**, H365 (2017).
21. B. R. Linter and G. T. Burstein, *Corros. Sci.*, **41**, 117 (1999).
22. S. Nešić, J. Postlethwaite, and S. Olsen, *Corrosion*, **52**, 280 (1996).
23. S. Nešić, N. Thevenot, J. L. Crolet, and D. Drazic, in *Corrosion*, Paper No. 03 (1996).
24. A. Kahyarian, B. Brown, and S. Nesic, *Corros. Sci.*, **129**, 146 (2017).
25. A. Kahyarian, B. Brown, and S. Nesic, *Corrosion*, **74**, 851 (2018).
26. A. A. El Miligy, D. Geana, and W. J. Lorenz, *Electrochim. Acta*, **20**, 273 (1975).
27. D. H. Davies and T. Burstein, *Corrosion*, **36**, 416 (1980).
28. E. B. Castro and J. R. Vilche, *Corros. Sci.*, **32**, 37 (1991).
29. S. Simard, M. Drogowska, H. Menard, and L. Brossard, *J. Appl. Electrochem.*, **27**, 317 (1997).
30. T. Tanupabrungsun, D. Young, B. Brown, and S. Nešić, in *Corrosion*, Paper No. 1418 (2012).
31. Z. Duan, R. Sun, C. Zhu, and I.-M. Chou, *Mar. Chem.*, **98**, 131 (2006).
32. T. H. M. Lal C. Garg, *Biochim. Biophys. Acta*, **261**, 70 (1971).
33. D. M. Kern, *J. Chem. Educ.*, **37**, 14 (1960).
34. D. A. Palmer and R. Van Eldik, *Chem. Rev.*, **83**, 651 (1983).
35. A. L. Soli and R. H. Byrne, *Mar. Chem.*, **78**, 65 (2002).
36. W. Stumm and J. J. Morgan, *Aquatic Chemistry: Chemical Equilibria and Rates in Natural Waters*, Third Edition., Wiley-Interscience, (1995).
37. X. Wang, W. Conway, R. Burns, N. McCann, and M. Maeder, *J. Phys. Chem. A*, **114**, 1734 (2010).
38. R. Alberty, *J. Phys. Chem.*, **99**, 11028 (1995).
39. J. Amri, E. Gulbrandsen, and R. P. Nogueira, *Corros. Sci.*, **52**, 1728 (2010).
40. K. F. Wissbrun, D. M. French, and A. Patterson Jr., *J. Phys. Chem.*, **58**, 693 (1954).
41. D. Pines et al., *J. Phys. Chem. B*, **120**, 2440 (2016).
42. A. Adamczyk, M. Prémont-Schwarz, D. Pines, E. Pines, and E. Nibbering, *Science*, **326**, 1690 (2009).
43. I. H. Plonski, *Int. J. Hydrogen Energy*, **21**, 837 (1996).
44. E. McCafferty and N. Hackerman, *J. Electrochem. Soc.*, **119**, 999 (1972).
45. A. Atkinson and A. Marshall, *Corros. Sci.*, **18**, 427 (1978).
46. F. Hibert, Y. Miyoshi, G. Eichkorn, and W. J. Lorenz, *J. Electrochem. Soc.*, **118**, 1919 (1971).
47. J. O. Bockris, D. Drazic, and A. R. Despic, *Electrochim. Acta*, **4**, 325 (1961).
48. O. E. Barcia and O. R. Mattos, *Electrochim. Acta*, **35**, 1601 (1990).
49. W. J. Lorenz, G. Staikov, W. Schindler, and W. Wiesbeck, *J. Electrochem. Soc.*, **149**, K47 (2002).
50. M. Keddam, O. R. Mattos, and H. Takenout, *J. Electrochem. Soc.*, **128**, 257 (1981).
51. M. Keddam, in *Corrosion Mechanisms in Theory and Practice,* Third Edition, Corrosion Technology., p. 149, CRC Press (2011).
52. D. M. Dražić, Iron and Its Electrochemistry in an Active State. In: Conway B.E., Bockris J.O., White R.E. (eds) *Modern Aspects of Electrochemistry*, vol 19. Springer, Boston, MA (1989).
53. K. E. Heusler, *Encyclopedia of Electrochemistry of the Elements. Vol.* ,**9** A. J. Bard, Editor, Marcel Dekker, New York, (1982).
54. M. Keddam, O. R. Mattos, and H. Takenout, *J. Electrochem. Soc.*, **128**, 266 (1981).
55. S. I. S. Douglas R. MacFarlane, *J. Electrochem. Soc.*, **133**, 2240 (1986).
56. F. M. Song, D. W. Kirk, J. W. Graydon, and D. E. Cormack, *Corrosion*, **60**, 736 (2004).
57. F. M. Song, D. W. Kirk, J. W. Graydon, and D. E. Cormack, *J. Electrochem. Soc.*, **149**, B479 (2002).
58. P. Lorbeer and W. J. Lorenz, *Corrosion*, **20**, 405 (1980).
59. J. Newman and K. E. Thomas-Alyea, *Electrochemical Systems*, 3rd ed., Wiley-interscience, (2004).
60. S. Aravinth, *Int. J. Heat Mass Transf.*, **43**, 1399 (2000).
61. Prabhata K. Swamee and Akalank K. Jain, "Explicit Equations for Pipe-Flow Problems." *Journal of the Hydraulics Division*. ASCE. Vol. 102, No. HY5, Proc. Paper 12146, May, 1976. pp. 657–664.
62. C. F. Colebrook and C. M. White, *Proc. R. Soc. A Math. Phys. Eng. Sci.*, **161**, 367 (1937).
63. W. Li, *Mechanical Effects of Flow on CO_2 Corrosion Inhibition of Carbon Steel Pipelines*, Ohio university, PhD. dissertation (2016).
64. W. Li, B. F. M. Pots, B. Brown, K. E. Kee, and S. Nesic, *Corros. Sci.*, **110**, 35 (2016).
65. E. S. Akeer, *Effect of Carbon Steel Composition and Microstructure on CO_2 Corrosion*, Ohio University, Masters Thesis (2014).
66. E. Akeer, B. Brown, and S. Nesic, Corrosion, Paper no. 2383, (2013).
67. D. Coleman, R. White, and D. Hobbs, *J. Electrochem. Soc.*, **142**, 1152 (1995).
68. D. Fan, *J. Electrochem. Soc.*, **138**, 1688 (1991).
69. K.-M. Yin, T. Yeu, and R. W. White, *J. Electrochem. Soc.*, **138**, 1051 (1991).
70. J. Newman, *Ind. Eng. Chem. Fundam.*, **7**, 514 (1968).
71. D. Li and Z. Duan, *Chem. Geol.*, **244**, 730 (2007).
72. Z. Duan and D. Li, *Geochim. Cosmochim. Acta*, **72**, 5128 (2008).
73. W. L. Marshall and E. U. Franck, *J. Phys. Chem. Ref. Data*, **10**, 295 (1983).
74. W. Wagner and H.-J. Kretzschmar, *International Steam Tables: Properties of Water*

and Steam based on the Industrial Formulation IAPWS-IF97, Second Edit., p. 169, Springer, (2008).

75. J. R. Cooper, Q. Mary, M. E. Road, and S. I. Associates, *Revised Release on the IAPWS Industrial Formulation 1997 for the Thermodynamic Properties of Water and Steam*, International Association for the Properties of Water and Steam, (2012).

76. E. Cussler, *Diffusion: Mass transfer in fluid systems*, Third Edit., Cambridge University Press, (2009).

77. W. M. Haynes, Ed., *CRC Handbook of Chemistry and Physics*, 84th ed., CRC Press LLC, (2004).

78. R. E. Zeebe and D. Wolf-Gladrow, *CO_2 in seawater: Equilibrium, kinetics, isotopes*, Elsevier, (2001).

79. M. Eigen, *Angew. Chem. Int. Ed. Engl.*, **3**, 1 (1964).

80. K. G. Schulz, U. Riebesell, B. Rost, S. Thoms, and R. E. Zeebe, *Mar. Chem.*, **100**, 53 (2006).

81. F. H. Stillinger, *Theor. Chem. Adv.*, **3**, 177 (1978).